Supporting Information for:

Dimensional Reduction of the Small-Bandgap Double Perovskite $Cs_2AgTlBr_6$

Bridget A. Connor,[a] Raisa-Ioana Biega,[b] Linn Leppert,*[b] and Hemamala I. Karunadasa*[a,c]

[a]Department of Chemistry, Stanford University, Stanford, California 94305, USA.
[b]Institute of Physics, University of Bayreuth, 95440 Bayreuth, Germany.
[c]Stanford Institute for Materials and Energy Sciences, SLAC National Accelerator Laboratory, Menlo Park, California 94025, USA.
*hemamala@stanford.edu, linn.leppert@uni-bayreuth.de

Table of Contents

Safety Warning

Thallium salts present a serious health hazard, which should not be taken lightly. Thallium exposure occurs most commonly through ingestion but can also occur through inhalation and skin contact. Early signs of acute Tl exposure include nausea and vomiting with symptoms progressing to include weakness, numbness, and pain in the hands and feet (peripheral neuropathy) followed by severe hair loss (alopecia) in later stages.[1] If exposure is suspected, seek medical attention immediately. To avoid exposure, proper personal protective equipment (PPE; gloves, safety glasses, lab coat, etc.) should always be worn when working with thallium. In addition, special care should be taken to ensure that gloves are solvent compatible as salts of Tl^{3+} are quite soluble in solvents like dimethylsulfoxide (DMSO), dimethylformamide (DMF), and acetone, which easily penetrate standard nitrile gloves. All manipulations of loose powders containing thallium should be performed in a fume hood to avoid inhalation.

In our lab, we have adopted standard procedures for working with thallium to minimize the risk of exposure. Thallium work is carried out only in designated and properly labeled work areas. Before beginning work, the work surface is covered with aluminum foil in order to contain spills. When possible, disposable lab supplies are used and discarded after contamination. In cases where this is not possible, we have set aside equipment designated for thallium use only. Non-disposable glassware contaminated with thallium is cleaned using aqua regia, rinsed thoroughly with water, then treated with dilute ammonium hydroxide (to remove AgX) and rinsed again with water followed by isopropanol. (Acetone should not be used to clean glassware as it can solubilize Tl salts and easily penetrate nitrile gloves.) After handling thallium-containing solids or solutions, gloves are disposed immediately. All solid thallium-contaminated waste is sealed in plastic Ziplock bags and collected separately from other lab waste. Similarly, thallium liquid waste is collected separately from other lab liquid waste.

Experimental Methods

All manipulations were conducted in air unless otherwise noted. Solvents were of reagent grade or higher purity. The solvent N,N′-dimethylformamide (DMF) was dried and degassed using the JC Meyer solvent purification system. All other reagents were purchased from commercial vendors and used as received. Crystals, powders, and films of $(BA)_4AgBiBr_8$ and $(BA)_2CsAgBiBr_7$ were synthesized as previously reported[2] unless otherwise noted. Abbreviations used: 3-BPA = 3-bromopropylammonium, BA = butylammonium, PEA = phenethylammonium, HIS = histammonium, Et_2O = diethyl ether HBr = hydrobromic acid.

$(3\text{-BPA})_4AgTlBr_8$ (1-Tl)

Crystals of **1-Tl** were prepared by combining Tl_2O_3 (122 mg, 0.267 mmol) and AgBr (252 mg, 1.34 mmol) with four equivalents of 3-bromopropylamine hydrobromide (485 mg, 2.22 mmol) in 1.4 mL of 9-M HBr. The mixture was heated for 12 h at 100 °C while stirring, forming a yellow solution. After this time, a large quantity of colorless solid remained undissolved. The hot solution was pipetted into a new vial, taking care to avoid the transfer of the undissolved solid. The solution was cooled to room temperature, leading to the formation of maroon plate-like crystals and some colorless powder. The solution was reheated to 100 °C, and the maroon crystals quickly re-dissolved, but the colorless solid remained undissolved even after several hours of heating. Once again, the hot solution was transferred to a new vial, avoiding undissolved material, and the solution was cooled to room temperature. The process was repeated one more time until only maroon crystals formed upon cooling to room temperature. Crystals of varying sizes and qualities could be prepared by cooling the solution at different rates. Those shown in main text Figure 1C were obtained by placing the hot solution on the benchtop to cool quickly to room temperature. Those suitable for ellipsometry (Figure S10) were obtained from a solution cooled at a controlled rate of 1 °C/h. Crystals were collected by filtration on a glass frit and dried under reduced pressure for 12 h, affording 350 mg of **1-Tl** (yield = 43.3%). Anal. Calcd. for $C_{12}H_{36}N_4AgBr_{12}Tl$: C: 9.56%, H: 2.41%, N: 3.72%. Found: C: 9.55%, H: 2.18%, N: 3.70%.

In general, crystals prepared as described above were not suitable for SCXRD analysis because those cooled at a slow rate were too large while those cooled quickly were of poor quality. This problem was resolved by cooling the initially formed yellow solution still containing the colorless precipitate from 100 °C to room temperature at a controlled rate of 3 °C/h. The undissolved colorless solid provided additional nucleation sites, leading to the formation of much smaller crystals. Single crystals of **1-Tl** were then isolated from the impurities in Paratone-N® oil and analyzed through SCXRD.

(PEA)$_2$CsAgTlBr$_8$ (2-Tl$_{PEA}$)

Powders of **2-Tl$_{PEA}$** were prepared by combining Tl_2O_3 (68 mg, 0.15 mmol), AgBr (223 mg, 1.19 mmol), and CsBr (116 mg, 0.545 mmol) with two equivalents of phenethylamine (75 μL, 0.59 mmol) in 5.3 mL of 9-M HBr. The mixture was heated for 12 h at 100 °C while stirring. After this time, all solids had dissolved, forming a yellow solution, but a small amount of black oil was present. The hot solution was filtered through glass microfiber filter paper to eliminate this oil and then reheated to 100 °C. The solution was cooled to room temperature at a controlled rate of 1 °C/h and then allowed to sit undisturbed at room temperature for two days. After this time, small black crystals formed at the bottom of the vial. The crystals were collected by filtration on a glass frit and dried under reduced pressure for 12 h, affording 129 mg of **2-Tl$_{PEA}$** (yield = 35.0%). Anal. Calcd. for $C_{16}H_{24}N_2AgCsBr_7Tl$: C: 15.39%, H: 1.94%, N: 2.24%. Found: C: 15.39%, H: 1.81%, N: 2.10%.

Crystallization. Crystals of **2-Tl$_{PEA}$** suitable for SCXRD were obtained by combining Tl_2O_3 (25 mg, 0.055 mmol), AgBr (63 mg, 0.34 mmol), and CsBr (23 mg, 0.11 mmol) with three equivalents of phenethylamine (41.8 μL, 0.331 mmol) in 0.5 mL of 9-M HBr. The mixture was heated for 4 h at 100 °C, affording a yellow solution with some remaining clumps of black and colorless solid. The solution was cooled from 100 °C at a controlled rate of 3 °C/h, yielding a mixture of flat, plate-like maroon (n = 1) and black (n = 2) crystals. The latter were isolated in Paratone-N® oil and analyzed by SCXRD. We were unable to consistently grow crystals of **2-Tl$_{PEA}$** suitable for ellipsometry measurements and therefore, these measurements were performed on the butylammonium analogue (**2-Tl$_{BA}$**).

(BA)$_2$CsAgTlBr$_8$ (2-Tl$_{BA}$)

Crystallization. Crystals of **2-Tl$_{BA}$** suitable for PXRD, elemental analysis, diffuse reflectance, and ellipsometry measurements were obtained by combining Tl_2O_3 (43 mg, 0.094 mmol), AgBr (90.3 mg, 0.48 mmol), and CsBr (53 mg, 0.25 mmol) with six equivalents of butylamine (111 μL, 1.12 mmol) in 0.75 mL of 9-M HBr. The mixture was heated for 18 h at 100 °C, yielding a yellow solution with some remaining clumps of colorless solid. The hot supernatant was separated from the solid into a new vial (preheated to 100 °C to avoid cooling the solution upon transfer) using a hot glass pipette. The solution was then cooled from 100 °C at a controlled rate of 1 °C/h, yielding flat, plate-like, black crystals. These crystals were harvested by filtration on a glass frit and dried under reduced pressure for 12 h. The crystals were carefully inspected under a microscope and separated from phase impurities also formed during the slow cool. Anal. Calcd. for $C_8H_{24}N_2AgCsBr_7Tl$: C: 8.33%, H: 2.10%, N: 2.43%. Found: C: 8.41%, H: 1.92%, N: 2.36%.

(HIS)$_2$AgTlBr$_8$ (1′-Tl)

Crystals of **1′-Tl** were prepared by combining Tl_2O_3 (93 mg, 0.20 mmol) and AgBr (77 mg, 0.41 mmol) with two equivalents of histamine (92 mg, 0.83 mmol) in 1.3 mL of 9-M HBr. The mixture was heated for 12 h at 100 °C while stirring, forming a yellow solution. After this time, a large quantity of colorless solid remained. The hot supernatant was pipetted into a new vial, taking care to avoid transferring the solid. The solution was cooled to room temperature, affording red-orange crystals and some colorless powder. The solution was reheated to 100 °C, and the red-orange crystals quickly re-dissolved, but the colorless solid remained even after several hours of heating. Once again, the hot supernatant was transferred to a new vial, avoiding undissolved material, and the solution was cooled to room temperature, leading to formation of only red-orange crystals. Crystals of varying sizes and qualities could be prepared by cooling the solution at different rates. Those shown in main text Figure 1D were obtained by allowing the hot solution to cool quickly to room temperature. Crystals were collected by filtration on a glass frit and dried under reduced pressure for 12 h, affording 295 mg of **1′-Tl** (yield = 61.3%). Anal. Calcd. for $C_{10}H_{22}N_6AgBr_8Tl$: C: 10.20%, H: 1.88%, N: 7.14%. Found: C: 10.27%, H: 1.91%, N: 7.01%.

In general, crystals prepared as described above were not suitable for SCXRD analysis because those cooled at a slow rate were too large whereas those cooled quickly were not of high enough quality. This problem was solved by cooling the initially formed yellow solution without separating it from the colorless precipitate from 100 °C to room temperature at a controlled rate of 3 °C/h. The undissolved colorless solid provided additional nucleation sites, leading to the formation of much smaller crystals. Single crystals of **1′-Tl** were then isolated from the phase impurities in Paratone-N® oil and analyzed by SCXRD.

(3-BPA)$_4$AgInBr$_8$ (1-In)

Crystals of **1-In** were prepared by combining In_2O_3 (23 mg, 0.083 mmol) and AgBr (32 mg, 0.17 mmol) with four equivalents of 3-bromopropylamine hydrobromide (145 mg, 0.662 mmol) in 0.5 mL of 9-M HBr. The mixture was stirred for 2 h at 100 °C, resulting in a clear colorless solution. The solution was cooled to room temperature, leading to the formation of colorless plate-like crystals. Crystals of varying sizes and qualities could be prepared by cooling the solution at different rates. Those shown in main text Figure 2B were obtained by allowing the hot solution to cool quickly to room temperature. Those suitable for SCXRD were obtained from a solution cooled at a controlled rate of 3 °C/h. Crystals were collected by filtration on a glass frit and dried under reduced pressure for 12 h, affording 134 mg of **1-In** (yield = 57.1%). Anal. Calcd. for $C_{12}H_{36}N_4AgBr_{12}In$: C: 10.17%, H: 2.56%, N: 3.95%. Found: C: 10.21%, H: 2.80%, N: 3.76%.

(BA)$_2$CsAgBiBr$_7$ (2-Bi)

Crystals of **2-Bi** suitable for ellipsometry were prepared by combining $BiBr_3$ (153 mg, 0.341 mmol), AgBr (64 mg, 0.341 mmol), and CsBr (73 mg, 0.343 mmol) with 17 equivalents of butylamine (572 µL, 5.79 mmol) in 2.9 mL of 9-M HBr. The mixture was stirred at 100 °C until a clear yellow solution was obtained (ca. 2 h). The stir bar was then removed from the solution (to eliminate additional nucleation sites) and the solution was cooled to room temperature at a controlled rate of 1 °C/h. The resulting large yellow rectangular plates were harvested by filtration on a glass frit and dried under reduced pressure for 12 h.

Thin-film deposition

Thin films were prepared by spin coating solutions of the perovskites onto glass or fused silica substrates. The substrates were first scrubbed with an aqueous Sparkleen® detergent solution, then sonicated for 10 minutes each in a bath of aqueous Sparkleen® detergent solution, deionized water, acetone, and then isopropanol. Then the substrates were blown dry with pressurized air and treated with a 15-minute UV-ozone etch immediately prior to film preparation.

*Thin-film deposition of **1-Tl***

Crystals of **1-Tl** (112 mg, 74 μmol) were dissolved in DMF (296 μL) and the resulting yellow solution was filtered through glass microfiber filter paper. The solution (20 μL) was deposited onto a glass substrate (1 cm^2) and spun at ca. 5,000 rpm for 20 s. The colorless film was quickly removed from the spin-coater and annealed at 100 °C for 2 minutes. During this annealing step, the film gradually turned orange.

*Thin-film deposition of **1′-Tl***

Crystals of **1′-Tl** (81 mg, 69 μmol) were dissolved in DMF (275 μL) and the resulting pale-yellow solution was filtered through glass microfiber filter paper. The solution (20 μL) was deposited onto a glass substrate (1 cm^2) and spun at ca. 5,000 rpm for 80 s. The colorless film was quickly removed from the spin-coater and annealed at 180 °C for 45 s. During this annealing step, the film turned yellow-orange.

*Thin-film deposition of **1-In***

Under an N_2 atmosphere, crystals of **1-In** (110 mg, 78 μmol) were dissolved in DMF (940 μL) and the resulting colorless solution was filtered through glass microfiber filter paper. The solution (20 μL) was deposited onto a fused silica substrate (1 cm^2) and spun at 3,000 rpm for 3 minutes while gently blowing N_2 into the top of the spin-coater. The colorless film was removed from the spin-coater and annealed at 70 °C for 3 minutes.

Crystal structure determination

Crystals were coated with Paratone-N® oil, mounted on a Kapton® loop, and transferred to a Bruker D8 Venture diffractometer equipped with a Photon 100 CMOS detector or to the Bruker D85 diffractometer at the Advanced Light Source beamline 11.3.1 or 12.2.1 at Lawrence Berkeley National Laboratory. Frames were collected using ω and φ scans and unit-cell parameters were refined against all data. The crystals did not show significant decay during data collection. Frames were integrated and corrected for Lorentz and polarization effects using SAINT 8.34a and were corrected for absorption effects using SADABS V2014.[3] Space-group assignments were based upon systematic absences, *E*-statistics, agreement factors for equivalent reflections, and successful refinement of the structures. Structures were solved using the intrinsic phasing method implemented in APEX2.[3, 4] Solutions were refined against all data using the SHELXTL-2013[5] software package and OLEX2.[4-7] Data for **2-Tl$_{\mathbf{PEA}}$** were treated as a non-merohedral twin using CELL_NOW. Hydrogen atoms were inserted at idealized positions and refined using a riding model with an isotropic thermal parameter 1.2 times that of the attached carbon or nitrogen atom. Thermal parameters for all non-hydrogen atoms were refined anisotropically. In the structures of **1-Tl** and **1-In**, portions of the organic molecules were refined using a disorder model. In **1-Tl**, **1-In**, and **2-Tl$_{\mathbf{PEA}}$**, additional disorder of the organic molecules was treated by restraining some C–C bond lengths and C–C–C bond angles and by restraining C atoms of the phenyl rings to lie in the same plane. Additionally, some C and N atoms were treated with rigid-bond and similar-ADP (atomic displacement parameter) restraints. Details regarding the data quality and a summary of the residual values of the refinements are listed in Table S1 and S2.

Crystal exfoliation

The top face of all crystals was exfoliated for single crystal ellipsometry and photoluminescence measurements as follows: a thin plate-like crystal was laid flat on a piece of double-stick tape fixed to a glass slide. A second piece of double-stick tape affixed to another glass slide was gently pressed on top of the crystal and then quickly removed by lifting straight up. With a few attempts, this process cleaved the crystal along the (001) plane, exposing a fresh, smooth, and highly reflective (001) face used for ellipsometry or photoluminescence measurements.

Ellipsometry measurements

General information. Spectroscopic ellipsometry measurements were obtained using a Horiba UVISEL phase modulated spectroscopic ellipsometer with a 75 W Xenon source. For all measurements, the angle of incidence was 69.85° and the spot size was 2.5 mm × 1 mm. The step size ranged from 1 nm to 5 nm. Before each measurement, the sample was aligned such that the reflected light spot was centered on the detector opening by adjusting the height and tilt of the sample stage. The rotation angle of the crystal with respect to an arbitrarily chosen initial orientation (defined as 0°) was measured using a protractor placed on the sample stage.

Data modeling. For many sample types that are commonly studied using ellipsometry (such as thin film samples), the resulting data must be extensively modeled in order to arrive at a physically meaningful description of the sample. This is because thin film samples have multiple interfaces which will reflect light back to the detector (i.e. the air-film interface and the film-substrate interface). Light reflected at these different interfaces has a different history resulting in unique polarizations and amplitudes of each reflected beam. The modeling procedure acts to separate these various reflected light beams and back out information about the sample based on the data. Fortunately, analysis of the raw ellipsometry data for **1-Tl**, **2-Tl$_{\mathbf{BA}}$**, **1-Bi**, and **2-Bi** is trivial compared to this because our measurements were carried out on exfoliated single-crystal samples thick enough that reflections from the back surface of the crystal are negligible. Thus, in all cases, our models assumed a single layer of infinite thickness with no surface roughness, good assumptions given the arguments presented below. All models were constructed using the New Amorphous dispersion formula. Other dispersion formulas (such as Tauc-Lorentz) did not yield significantly different results.

No surface roughness. Initially, the materials were treated as having two layers: a surface layer consisting of a mixture of void and perovskite to model surface roughness and a second layer consisting of a perovskite slab of infinite thickness. However, in general, model refinement led to a result indicative of little to no surface roughness and eliminating the top layer had no substantial effect on the fit. This is unsurprising given that the top surface of the crystals was exfoliated prior to measurement, exposing highly smooth and reflective faces. Therefore, in all cases, the assumption of no surface roughness is a good one.

Infinite thickness. In our measurements, we are primarily concerned with absorption coefficients $>10^4$ cm^{-1} since below this value, our plots of α vs. energy obtained from ellipsometry essentially reach a baseline. For an absorption coefficient of 10^4 cm^{-1}, 99% of the light that enters the sample (rather than being reflected from its top surface) is absorbed over a path length of 4.6 μm. Light that enters the crystal can only reach the detector after reflecting off the bottom face of the crystal and thus, must traverse the crystal twice. The path length that the light must travel within the crystal is determined by

> the angle of incidence. In our ellipsometry setup, light is incident upon the crystal at an angle ca. 70° with respect to the surface normal. Assuming an index of refraction of 2 (close to the maximum value measured for our materials), light enters the crystal with an angle of incidence of ca. 28°. Under these conditions, a crystal that is ca. 2 μm thick requires light to travel 2.3 μm to reach the bottom face of the crystal and is therefore, sufficiently thick to absorb 99% of the light (for $\alpha = 10^4$ cm^{-1}). In reality, under these conditions, even less than 1% of the light initially entering the crystal will reach the detector because we have not accounted for the fraction of light that is reflected/transmitted at each interface (i.e., the crystal's back and front faces). Since the crystals we used for ellipsometry measurements were on the order of tens of microns thick, for absorption coefficients $>10^4$ cm^{-1} the quantity of light that reflects off the back face and reaches the detector is negligible, meaning that our approximation of infinite thickness is a good one.

Data for **1-Tl** and **2-Tl$_{\mathbf{BA}}$** were fit using models with four and three oscillators, respectively. Fitting yielded values for the parameter n_∞ which corresponds to the value of n (the refractive index) when ω (photon energy) → ∞ for **1-Tl** (1.57 for **1-Tl$_{\mathbf{0}}$** and 1.56 for **1-Tl$_{\mathbf{90}}$**) and **2-Tl$_{\mathbf{BA}}$** (1.73). Data modeling for **1-Bi** and **2-Bi** was substantially more challenging, likely due to the sharpness of the spectral features. Using a single oscillator, we were able to fit a portion of the lowest energy absorption feature in both spectra. However, our attempts to model a larger portion of the spectrum invariably led to models that were either very poor fits to the experimental data or which contained unphysical parameters such as oscillators with negative intensities. Given these difficulties with modeling, we chose to extract the values of n (refractive index) and k (extinction coefficient) through direct inversion of the raw data. This is valid given that the crystals of **1-Bi** and **2-Bi** can be reasonably approximated as having no surface roughness and infinite thickness. Because reliable data modeling for the Ag–Bi was not possible, we were unable to extract values for the parameter n_∞ for these materials. Note that Figures S17-S20 plot n as a function of energy for **1-Tl**, **2-Tl$_{\mathbf{BA}}$**, **1-Bi**, and **2-Bi**.

To compare the optical constants obtained through data modeling and through direct inversion of the raw data, in Figure S6, we show plots of α vs. energy for **1-Bi** for the case where (1) only the lowest-energy portion of the raw data was fit, (2) the entire range of data was fit but using a model containing oscillators with unphysical parameters, and (3) k was extracted by direct inversion of the raw data. All plots look essentially identical. Furthermore, for the case where k was obtained through direct inversion of the raw data, the plot of α vs. energy has a shape nearly identical to that obtained from thin-film absorption measurements for both **1-Bi** and **2-Bi**. Figure 3B and Figure S7 show that the shape of the thin-film transmission spectrum of **1-Bi** is nearly identical to the plots of α vs. energy obtained from ellipsometry. The thin-film absorption spectrum of **2-Bi** is also very similar to the plots of α vs. energy obtained from ellipsometry measurements (Figure S8). The good agreement of the spectral shape obtained through two very different methods lends credence to our modeling decisions.

Orientational dependence. Since ellipsometry employs polarized light and because all materials are anisotropic, crystals were measured in several different orientations. The spectra of **1-Bi**, **2-Bi**, and **2-Tl$_{\mathbf{BA}}$** did not vary significantly with orientation as shown in Figures S7-S9. Here, spectra obtained in three different orientations are shown: an initial (arbitrary) orientation (defined as 0°) and orientations in which the crystals were rotated by 45° and 90° with respect to this initial orientation. In all cases, the position and magnitude of peaks changed very little in these different orientations and in all cases, we have selected just one of these spectra to represent each material in main text Figure 3A,B,C. As discussed in the main text, the ellipsometry spectrum of **1-Tl** *does* vary substantially with orientation. We find a smooth variation in the spectrum between the two unique orientations defined as 0□ (**1-Tl**$_{\mathbf{0}}$) and 90□ (**1-Tl**$_{\mathbf{90}}$), as shown in Figure S10. Taken alone, neither of the two unique optical spectra (**1-Tl**$_{\mathbf{0}}$ or **1-Tl**$_{\mathbf{90}}$) match the thin-film transmission spectrum of **1-Tl** (Figure S11) but their average gives a good match (Figure 3D), as expected.

Peak width analysis. The peak width analysis of the plots of α vs. energy for **1-Tl** and **2-Tl**$_{\mathbf{BA}}$ discussed in the main text were performed using the modeled ellipsometry data. Our models for each material consisted of several oscillators described by Equation S1, where the intensity, broadening, and position of each oscillator are described by the parameters f_j, Γ_j, and ω_j, respectively. For both **1-Tl** and **2-Tl**$_{\mathbf{BA}}$, the low-energy absorption feature was mostly described by one oscillator (Figure S14-S16). Thus, to compare the width of these features in **1-Tl** and **2-Tl**$_{\mathbf{BA}}$, we compare the broadening parameters (Γ_j) of these oscillators. As described in the main text and illustrated in Figure 3C, the ellipsometry spectrum of a crystal of **1-Tl** varies as the crystal is rotated, and we refer to the two unique spectra obtained at rotation angles of 0° and 90° as **1-Tl**$_{\mathbf{0}}$ and **1-Tl**$_{\mathbf{90}}$, respectively. The broadening parameter for **2-Tl**$_{\mathbf{BA}}$ is ca. 41% larger than that for **1-Tl**$_{\mathbf{0}}$ and ca. 19% larger than that for **1-Tl**$_{\mathbf{90}}$ (Table S5).

Since we had substantial difficulty fitting the raw ellipsometric data for **1-Bi** and **2-Bi**, instead of comparing broadening parameters obtained from modeled ellipsometry data, we took the spectra in which n and k were obtained through direct inversion of the data and fit the low-energy feature to a Pseudo-Voigt function (Equation S2). The resulting fits and the fit parameters are shown in Figure S12-S13 and Table S6, respectively. The width parameter (w) for the lowest-energy feature is nearly identical in the spectra of both **1-Bi** and **2-Bi** (0.287 and 0.286, respectively).

Absorption measurements

Absorption measurements of thin films and powders ground in Paratone-N® oil were taken using an Agilent Cary 6000i spectrometer. For thin-film transmission measurements of **1-Tl**, **1′-Tl**, **1-In**, **1-Bi**, and **2-Bi**, the film was placed directly in the beam path and the instrument was operated in transmission mode. For integrating sphere measurements, the instrument was equipped with the diffuse reflectance accessory. A thin-film absorption spectrum of **2-Bi** was obtained with the film mounted in the center of the integrating sphere and the instrument operating in absorbance mode. Powder samples of **1-Tl**, **1′-Tl**, **2-Tl**$_{\mathbf{PEA/BA}}$, **1-Bi**, and **2-Bi** were prepared for diffuse reflectance measurements by pulverizing a small crystal of each material in Paratone-N® oil. Grinding in oil protected the samples from moisture and yielded small particles. A thin layer of the oil suspension was deposited on a glass slide and mounted in the center of the integrating sphere. The instrument was operated in reflectance mode and the obtained spectra were converted to pseudo-absorbance spectra using the Kubelka-Munk transformation (Figure S1-S4).[8] Powders of **1-In** were ground in a mortar and pestle then mixed with $BaSO_4$ to make a dilute mull that was then pressed into a pellet of $BaSO_4$ and used for diffuse reflectance measurements (Figure S5) obtained on a Shimadzu UV-2600 spectrometer equipped with an integrating sphere.

A note on absorption onsets in ellipsometry, thin-film transmission, and diffuse reflectance data. As mentioned in the main text, ellipsometry and thin-film transmission measurements are only sensitive to strong absorption events. Thus, the absorption onsets observed in these spectra do not necessarily correspond to the bandgap onset because weak absorption from indirect or symmetry-forbidden direct gaps (with absorption coefficients <10^4 cm^{-1}) are not evident. Diffuse reflectance spectra are more sensitive to weak absorption events. However, lattice defects and disorder,[2] indirect transitions,[2] and symmetry-forbidden direct transitions[9] can all give rise to weak low-energy absorption in halide double perovskites, complicating the unambiguous assignment of such absorption. Figures S2-S5 demonstrate that diffuse reflectance measurements give a lower energy absorption onset than thin-film/ellipsometry measurements for **1-Tl**, **2-Tl$_{BA}$**, **1'-Tl**, and **1-In**. However, an in-depth investigation into the source of the weak low-energy absorption in **1-Tl**, **2-Tl$_{BA}$**, **1'-Tl**, and **1-In** (similar to that conducted in our previous work for **1-Bi**[2]) is not the focus of the present work. It is also important to note that a Tauc analysis[10] of the diffuse reflectance spectra, which was developed for materials with a 3D density of states (DoS), should not be used to determine the indirect/direct nature of the bandgap of layered perovskites with a 2D DoS (Figure S25).

Photoluminescence (PL) measurements

PL measurements of **1-Tl** and **2-Tl$_{BA}$** were conducted on large exfoliated crystals using a Horiba LabRAM ARAMIS Raman microscope equipped with a 532 nm laser with a spot size of ca. 10 μm and operating at a power ranging from 0.036 mW to 3.6 mW. No PL or visible surface damage was observed at any of these laser powers. PL measurements of **1′-Tl** were conducted on a large crystal mounted on a glass slide using a Horiba Jobin-Yvon NanoLog fluorimeter equipped with a 450 W xenon lamp and a DM302 UV/vis detector. The excitation wavelength was varied from 350 nm to 450 nm, but in all cases, no emission was detected. PL measurements of **1-In** were conducted using the same setup on a powder pressed onto a piece of black optical tape. The excitation wavelength was varied from 275 nm to 350 nm, but in all cases, no emission was detected.

Other physical measurements

Powder X-ray diffraction (PXRD) measurements were performed on a Bruker D8 Advance diffractometer equipped with a Cu anode, fixed divergence slits with a nickel filter, and a LYNXEYE 1D detector. The instrument was operated in a Bragg-Brentano geometry with a step size of 0.02° (2θ) or less. Simulated powder patterns were calculated using the crystallographic information files (CIFs) from single-crystal X-ray experiments. C, H, and N analyses were performed by MHW Laboratories (Phoenix, AZ) (**1-In**) or Elemental Analysis Incorporated (**1-Tl**, **2-Tl$_{PEA/BA}$**, and **1′-Tl**).

Computational Details:

To understand the differences in electronic structure between the Ag–Tl and Ag–Bi families of double perovskites, we carried out first principles density functional theory (DFT) calculations for $Cs_2AgTlBr_6$, **1-Tl**, **2-Tl$_{PEA}$**, **1′-Tl, 1-In**, **1-Bi**, and **2-Bi** using both the experimentally determined SCXRD structures as well as a number of model systems. All calculations were performed using VASP[11, 12] and projector augmented wave (PAW) potentials.[13] The PAW pseudopotentials have the following atomic configurations: $5s^25p^66s^1$ for Cs, $6s^26p^1$ for Tl, $4d^{10}5s^1$ for Ag, $6s^26p^3$ for Bi, $5s^25p^1$ for In, $4s^24p^5$ for Br, $2s^22p^2$ for C and $2s^22p^3$ for N. We used *k*-point grids with 4 × 4 × 4 points for $Cs_2AgTlBr_6$ and 2 × 2 × 1 points for **1-Tl**, **2-Tl$_{PEA}$**, **1′-Tl, 1-In**, **1-Bi**, **2-Bi** and a cutoff energy for the plane-wave expansion of 500 eV. Using these parameters, our bandgaps are converged to within 50 meV.

For **1-Bi** and **2-Bi**, the calculations were performed using the exchange-correlation (xc) functional of Perdew, Burke and Ernzerhof (PBE)[14] and including the effect of spin-orbit coupling (SOC) self-consistently as in ref. 2. While the VB, which has Ag d, Bi s and Br p character, is almost unaffected by

SOC, the CB changes substantially. For both **1-Bi** and **2-Bi** systems, the inclusion of SOC introduces a large spin-orbit splitting between the $J = 1/2$ and $J = 3/2$ bands.[2]

Semilocal approximations to the xc functional are known to underestimate bandgaps. However, the most important features of the band structure and bandgap and dispersion trends are generally reproduced very well. A notable exception is the case of $Cs_2AgTlBr_6$, for which PBE predicts a "negative" bandgap, pushing the conduction band minimum (CBM) below the valence band maximum (VBM).[9] We therefore used the screened hybrid functional of Heyd, Scuseria and Ernzerhofer (HSE06)[15] for all members of the Ag–Tl double perovskite family and for **1-In** (Table S7). The HSE06 bandgap of $Cs_2AgTlBr_6$ is 0.12 eV, still underestimating the experimental gap by ~0.8 eV but correctly predicting the material to be a semiconductor. Qualitatively accurate bandgaps can be obtained by using the GW approach.[16] We note that in order to obtain bandgaps that are similar in magnitude to the experimentally observed absorption onsets of our materials, electron-hole interactions have to be taken into account, e.g., by solving the Bethe-Salpeter equation for the correlated electron-hole amplitude. Nevertheless, the trend in the magnitudes of our calculated bandgaps (i.e., $Cs_2AgTlBr_6$ < **2-Tl$_{\mathbf{PEA}}$** < **1-Tl** < **1′-Tl** < **1-In**) matches the experimentally observed trend in absorption onsets for these materials (see Table S7 and Figures 2B,3C). The calculations for $Cs_2AgTlBr_6$, **1-Tl**, **2-Tl$_{\mathbf{PEA}}$**, **1′-Tl**, and **1-In** have been performed without taking into account the effect of SOC. The exclusion of SOC from these calculations is justified by the fact that the CBM of all the Ag–Tl and Ag–In perovskites studied here has mainly s-orbital character while the VBM has mainly Ag d-orbital character. Consequently, the inclusion of SOC leads to bandgap changes of less than 0.1 eV and no appreciable changes in band dispersion.

Band structures of $Cs_2AgTlBr_6$, 1-Tl, and 2-Tl$_{\mathbf{PEA}}$:

The HSE06 band structure of $Cs_2AgTlBr_6$ exhibits a direct gap of 0.12 eV at Γ. The VBM is composed of Ag d and Br p orbital contributions and the CBM has Ag s, Tl s and Br p character (Figure 4A). The CB is highly disperse due to the overlap of spherical Tl^{3+} 6s orbitals with the halide p orbitals, as described in ref. 11. The band structure of **2-Tl$_{\mathbf{PEA}}$** shows a similar orbital composition of the VB and CB, a direct bandgap at Γ, and similar overall band dispersion (Figure 4C).

The band structure of **1-Tl** differs substantially from that of $Cs_2AgTlBr_6$ and **2-Tl$_{\mathbf{PEA}}$** (Figure 4D). Most notably, it exhibits an indirect bandgap of 2.00 eV between the VBM at $A = (^{\pi}/_{a}, ^{\pi}/_{b}, 0)$ and the CBM at $B = (^{\pi}/_{a}, 0, 0)$ as calculated with HSE06. The bandgap between A and Γ is 113 meV higher in energy. In **1-Tl**, the VBM is composed almost entirely of Br p and Ag d orbitals and the CBM consists primarily of Tl s and Br p orbitals. Thus, metal orbital contributions at both band edges in **1-Tl** come predominantly from just one of the two unique B-site cations.

Band structures of undistorted model Ag–Tl perovskites:

In order to separate the effects of structural distortions from those of the reduced dimensionality on the band structures of **1-Tl** and **2-Tl**, we constructed undistorted model systems (using untilted and undistorted metal-halide octahedra, as found in the parent 3D lattice) with layer thicknesses of $n = 1$ and 2 (**1M** and **2M**, respectively). These model systems were constructed with Tl–Br and Ag–Br bond lengths of 2.73 Å and 2.81 Å, respectively, corresponding to the length of Tl–Br and Ag–Br bonds in the experimental structure of $Cs_2AgTlBr_6$. For simplicity, in these model structures, the organic molecules have been replaced by Cs cations using the stoichiometry $Cs_{2n+2}Ag_nBi_nBr_{2(3n+1)}$. To avoid spurious interactions between periodic images, a vacuum layer of at least 20 Å was introduced between the perovskite layers and a dipole correction was applied in all calculations.

Similar to **1-Tl** and **2-Tl$_{\text{PEA}}$**, **1M** and **2M** exhibit an indirect and direct bandgap, respectively (Figure S23), indicating that the transition from a direct bandgap in materials with $n > 1$ to an indirect bandgap for $n = 1$ depends mostly on the thickness of the inorganic layer. However, there are some differences in the band dispersion between the model and experimental systems, demonstrating that structural distortions play an important role in determining the shape of the bands. For example, in moving from **1-Tl** to **1M**, the CBM shifts from B to Γ, leaving the A→Γ transition as the lowest-energy excitation. It is also worth noting that the bandgaps of the model systems are lower than those of the corresponding experimental structures due to the impact of structural distortions (Table S8).

We also constructed an undistorted model structure with $n = 3$ and then relaxed this structure using the PBE functional with van der Waals corrections computed using the methods of Tkatchenko and Scheffler.[17] The band structure of this relaxed model $n = 3$ structure (calculated with HSE06) is completely analogous to those of $Cs_2AgTlBr_6$ and **2-Tl$_{\text{PEA}}$** (Figure 4B), suggesting that all materials with $1 < n < \infty$ have analogous band structures.

Band structure of 1-In:

As expected, the band structure of **1-In** (Figure S24) is similar to that of isoelectronic **1-Tl**. **1-In** displays an indirect bandgap between A = $(^{\pi}/_{a}, ^{\pi}/_{b}, 0)$ in the VB and Γ in the CB of 3.30 eV. The indirect bandgap between A and B = $(^{\pi}/_{a}, 0, 0)$ is 93 meV higher in energy. The HSE06 bandgap of **1-In** is ~1.3 eV larger than that of **1-Tl**, this agrees well with our experimental findings of a substantially blueshifted (by ca. 1.4 eV) absorption onset in **1-In** relative to **1-Tl** (Figure 2B).

Notably, as in the Ag–Tl family of double perovskites, in the Ag–In family, we observe a substantial difference in band structure between the 3D and $n = 1$ members. Computational studies of $Cs_2AgInCl_6$, the closest experimentally synthesized 3D analogue to **1-In**, indicate that this material has a direct bandgap at Γ.[18] Thus, in the Ag–In system we also find a transition from a direct bandgap in the 3D structure to an indirect bandgap in the $n = 1$ material.

Band structure of 1′-Tl:

The crystal structure of **1′-Tl** is best solved in the space group *C*2/*c* where each unit cell contains four formula units. However, using this crystal structure as a starting point for our calculations leads to band folding as this monoclinic unit cell is not the primitive unit cell of the lattice. We therefore solved the crystal structure in the lower-symmetry space group *P*-1, in which each unit cell contains two formula and used this as a starting point for our computational studies. Notably, no significant structural differences are observed between these lower- and higher-symmetry solutions, indicating that the differences in the band structures obtained using these two different starting points are artifacts caused by the larger unit cell of the higher-symmetry structure.

The quasi-1D **1′-Tl** system exhibits an indirect bandgap of 2.17 eV between the VBM at V= $(^{\pi}/_{a}, ^{\pi}/_{b}, 0)$ and the CBM at Γ (Figure 4E). The VBM is composed of Ag d and Br p orbitals and the CBM has Tl s and Br p character. The increased bandgap (by ca. 170 meV, Table S7) calculated for **1′-Tl** relative to **1-Tl** is consistent with the experimentally observed blueshift (by ca. 220 meV, Figure 2B) in the transmission spectrum of **1′-Tl** relative to **1-Tl**. We also find that the bands of **1′-Tl** are less disperse than those of **1-Tl**, as expected due to the lower dimensionality of the inorganic lattice in **1′-Tl**.

Equivalence of the V and X points of the triclinic lattice of 2-Tl$_{\mathrm{PEA}}$ to the X and L points, respectively, of the cubic *Fm*−3*m* lattice of $Cs_2AgTlBr_6$

Previously, we demonstrated that the band structures of 3D $Cs_2AgBiBr_6$ and 2D $(BA)_2CsAgBiBr_7$ (**2-Bi**) are analogous by showing that the *k*-points at which the VBM and CBM occur in $Cs_2AgBiBr_6$ (X and L, respectively) are the translational symmetry equivalents of the *k*-points at which the VBM and CBM occur in the 2D material (A and B, respectively, Figure S26). The reciprocal space coordinates of a given *k*-point dictate the translational symmetry rules for that *k*-point (i.e., whether the wavefunction undergoes a symmetric or antisymmetric translation along each of the real space unit cell vectors). Thus, in order to determine how the translational symmetry of *k*-points in the *Fm*–3*m* lattice of $Cs_2AgBiBr_6$ can be converted to equivalent translational symmetry rules for the 2D *P*2$_1$/*m* lattice of **2-Bi**, we expressed the two in-plane unit cell vectors ($\boldsymbol{a}$ and $\boldsymbol{b}$) of **2-Bi** (Figure S27A) in terms of the primitive unit cell vectors of $Cs_2AgBiBr_6$ ($\boldsymbol{x}$, $\boldsymbol{y}$, and $\boldsymbol{z}$). The 2D translational symmetry rules derived in this way enabled us to find the *k*-points in the reciprocal lattice of the 2D material corresponding to those rules. (For the full procedure, we refer the reader to the Supporting Information of our previous publication).[2]

We can use this same reasoning to relate the *k*-points of the *Fm*–3*m* lattice of 3D $Cs_2AgTlBr_6$ to the *k*-points of the *P*–1 lattice of 2D $(PEA)_2CsAgTlBr_7$ (**2-Tl$_{\mathrm{PEA}}$**). As shown in Figure S27B, the $\boldsymbol{a}$ and $\boldsymbol{b}$ unit cell vectors of **2-Tl$_{\mathrm{PEA}}$** lie in the plane of the inorganic sheets and bisect Br–M–Br (M = Ag, Tl) angles to connect metal centers of the same type, while the $\boldsymbol{c}$ vector points between adjacent inorganic sheets. These unit cell vectors are analogous to those of **2-Bi** (Figure S27A). Therefore, the same expressions we found previously relating the primitive $\boldsymbol{x}$, $\boldsymbol{y}$, and $\boldsymbol{z}$ unit cell vectors of a cubic *Fm*–3*m* lattice to the two in-plane $\boldsymbol{a}$ and $\boldsymbol{b}$ unit cell vectors of a 2D derivative are valid.

$$\boldsymbol{a} = \boldsymbol{x}$$

$$\boldsymbol{b} = \boldsymbol{y} - \boldsymbol{z}$$

As a result, the 2D translational symmetry rules (and therefore the reciprocal space coordinates) we derived for the *P*2$_1$/*m* lattice of **2-Bi** from various *k*-points of the *Fm*–3*m* lattice also apply to the *P*–1 lattice of **2-Tl$_{\mathrm{PEA}}$**. The only difference between the *P*2$_1$/*m* and *P*–1 cases is in the labeling of the *k*-points. For example, we previously found that the *Fm*–3*m* *k*-point X, with reciprocal lattice coordinates $(^{\pi}/_{a}, 0, ^{\pi}/_{a})$, is equivalent to a *k*-point in the 2D reciprocal lattice with coordinates along the reciprocal lattice vectors $\boldsymbol{k_a}$ and $\boldsymbol{k_b}$ of $(^{\pi}/_{a}, ^{\pi}/_{b})$. In the case of the primitive monoclinic lattice, this corresponds to the A point. For the triclinic *P*–1 lattice, these coordinates correspond to the point labeled as V $((^{\pi}/_{a}, ^{\pi}/_{b}, 0))$. Thus, the X point of the *Fm*–3*m* lattice is the translational symmetry equivalent of the V point in the *P*–1 lattice of **2-Tl$_{\mathrm{PEA}}$** (Figure S26). Likewise, we found that the *Fm*–3*m* *k*-point L, with reciprocal lattice coordinates $(^{\pi}/_{a}, ^{\pi}/_{a}, ^{\pi}/_{a})$, is equivalent to a *k*-point in the 2D reciprocal lattice with coordinates along the reciprocal lattice vectors $\boldsymbol{k_a}$ and $\boldsymbol{k_b}$ of $(^{\pi}/_{a}, 0)$. For a primitive monoclinic lattice, this corresponds to the B point. For the triclinic *P*–1 lattice of **2-Tl$_{\mathrm{PEA}}$**, this corresponds to the point labeled as X $((^{\pi}/_{a}, 0, 0))$. Thus, the L point of the *Fm*–3*m* lattice is the translational symmetry equivalent of the X point in the *P*–1 lattice of **2-Tl$_{\mathrm{PEA}}$** (Figure S26).

Table S1. Crystallographic data for $(HIS)_2AgTlBr_8$ (**1′-Tl**) and $(3\text{-}BPA)_4AgTlBr_8$ (**1-Tl**).

	$(HIS)_2AgTlBr_8$	**$(3\text{-}BPA)_4AgTlBr_8$**
Empirical Formula	$C_{10}H_{22}AgBr_8N_6Tl$	$C_{12}H_{36}AgBr_{12}N_4Tl$
Formula Weight, g/mol	1177.85	1507.61
Temperature, K	295	298
Crystal System	Monoclinic	Monoclinic
Space group	$C2/c$	$P2/c$
a, Å	11.3098(4)	8.4673(3)
b, Å	12.6075(5)	7.8406(3)
c, Å	18.2063(7)	26.1647(10)
β, °	95.713(2)	90.312(2)
Volume, Å^3	2583.11(17)	1737.02(11)
Z	4	2
Density (calculated), g/cm^3	3.029	2.882
Absorption coefficient, mm^{-1}	20.540	20.160
$F(000)$	2128.0	1368.0
Crystal size, mm^3	0.45 × 0.28 × 0.1	0.13 × 0.07 × 0.01
Radiation	Synchrotron (λ = 0.7288 Å)	Synchrotron (λ = 0.7288 Å)
2θ range, °	4.976 to 52.084	3.192 to 55.15
Index ranges	$-13 \leq h \leq 13$ $-15 \leq k \leq 15$ $-21 \leq l \leq 21$	$-10 \leq h \leq 10$ $-9 \leq k \leq 9$ $-33 \leq l \leq 33$
Reflections collected/unique	17647/2360	28564/3727
Completeness to θ_{max}	0.996	0.999
Max. and min. transmission	0.108, 0.027	0.431, 0.270
Data/restraints/parameters	2360/0/122	3727/3/158
Goodness-of-fit on F^2	1.126	1.082
Final R indices $[I > 2\sigma(I)]^a$	R_1 = 0.0496 wR_2 = 0.1036	R_1 = 0.0380 wR_2 = 0.0862
R indices (all data)^a	R_1 = 0.0500 wR_2 = 0.1041	R_1 = 0.0495 wR_2 = 0.0905
Largest diff. peak and hole, e/Å^{-3}	1.53, –1.72	1.08, –1.01

$^aR_1 = \Sigma||F_o| - |F_c||/\Sigma|F_o|$, $wR_2 = [\Sigma w(F_o^2 - F_c^2)^2/\Sigma(F_o^2)^2]^{1/2}$

Table S2. Crystallographic data for $(3\text{-BPA})_4AgInBr_8$ (**1-In**) and $(PEA)_2CsAgTlBr_7$ (**2-Tl$_{PEA}$**).

	$(3\text{-BPA})_4AgInBr_8$	**$(PEA)_2CsAgTlBr_7$**
Empirical Formula	$C_{12}H_{36}AgBr_{12}InN_4$	$C_{16}H_{24}AgBr_7N_2Tl$
Formula Weight, g/mol	1418.06	1248.89
Temperature, K	296.15	298
Crystal System	Monoclinic	Triclinic
Space group	*P*2/*c*	*P*-1
a, Å	8.4965(5)	7.8617(6)
b, Å	7.8419(5)	7.8687(6)
c, Å	26.1413(17)	23.0185(11)
α, °	90	83.703(5)
β, °	90.318(2)	85.727(5)
γ, °	90	89.818(6)
Volume, Å^3	1741.73(19)	1411.41(17)
Z	2	2
Density (calculated), g/cm^3	2.704	2.939
Absorption coefficient, mm^{-1}	15.000	16.177
F(000)	1304.0	1124.0
Crystal size, mm^3	0.375 × 0.215 × 0.05	0.32 × 0.17 × 0.01
Radiation	MoKα (λ = 0.71073 Å)	Synchrotron (λ = 0.6888 Å)
2θ range, °	4.794 to 50.694	3.46 to 49.184
Index ranges	$-10 \leq h \leq 10$ $-9 \leq k \leq 9$ $-31 \leq l \leq 31$	$-9 \leq h \leq 9$ $-9 \leq k \leq 9$ $0 \leq l \leq 27$
Reflections collected/unique	26239/3193	5124/5124
Completeness to θ_{max}	1.000	0.980
Max. and min. transmission	0.430, 0.111	0.291, 0.121
Data/restraints/parameters	3193/33/150	5124/184/256
Goodness-of-fit on F^2	1.112	1.071
Final *R* indices [$I > 2\sigma(I)$]^a	$R_1 = 0.0599$ $wR_2 = 0.1573$	$R_1 = 0.0661$ $wR_2 = 0.1745$
R indices (all data)^a	$R_1 = 0.0684$ $wR_2 = 0.1641$	$R_1 = 0.0882$ $wR_2 = 0.1934$
Largest diff. peak and hole, e/Å^{-3}	1.50, –1.33	1.69, –2.31

$^aR_1 = \Sigma||F_o| - |F_c||/\Sigma|F_o|$, $wR_2 = [\Sigma w(F_o^2 - F_c^2)^2/\Sigma(F_o^2)^2]^{1/2}$

Table S3. Selected bond lengths, bond angles, and distortion parameters for **1-Bi**, **1-Tl**, and **1-In** demonstrating the structural similarity of these materials.

	(BA)$_4$AgBiBr$_8$ (1-Bi)	**(3-BPA)$_4$AgTlBr$_8$ (1-Tl)**	**(3-BPA)$_4$AgInBr$_8$ (1-In)**
Ag–Br$_{ax}$ bond length (Å)	2.6156(1)	2.5665(1)	2.5565(2)
Ag–Br$_{eq}$ bond length (Å)	3.0608(1)	3.1421(1), 3.0576(1)	3.2060(1), 3.1257(1)
Br$_{eq.}$–Ag–Br$_{eq.}$ angle (°)	94.670(1), 85.330(1)	100.086(1), 96.959(1), 81.478(1), 81.478(1)	80.960(2), 80.960(2), 98.074(2), 100.008(2)
Br$_{eq.}$–Ag–Br$_{ax.}$ angle (°)	89.383(2), 90.617(2)	91.519(1), 94.306(1), 88.400(1), 85.956(1)	94.249(2), 91.190(2), 86.081(2), 88.587(2)
Ag–Br–B angle (°, B = Bi, Tl, In)	166.868(2)	164.847(1), 163.607(1)	164.223(2), 163.469(2)
Ag–Br octahedral distortion factor[1]	5.1×10^{-3}	7.5×10^{-3}	9.5×10^{-3}
B–Br octahedral distortion factor (B = Bi, Tl, In)[*]	3.3×10^{-6}	4.1×10^{-5}	2.0×10^{-5}

---

[*] Mean-square relative deviation of M–Br bond lengths from the average: $\Delta = \frac{1}{6}\sum_{n=1}^{6}\left[\frac{d_n-d}{d}\right]^2$

Table S4. Bond lengths of **2-Tl$_{\mathrm{PEA}}$** and **2-Bi** demonstrating the similar structural distortions of these perovskites.

	Bond Type			**Bond Length (Å)**
(PEA)$_2$CsAgTlBr$_7$	Ag–Br	Axial	Terminal Br	2.6699(1)
			Bridging Br	3.0826(2)
		Equatorial		2.8420(2), 2.8451(2), 2.9014(2), 2.8393(2)
	Tl–Br	Axial	Terminal Br	2.6985(1)
			Bridging Br	2.6818(1)
		Equatorial		2.7332(2), 2.7342(2), 2.7493(2), 2.7617(2)
(BA)$_2$CsAgBiBr$_7$	Ag–Br	Axial	Terminal Br	2.6514(1)
			Bridging Br	3.0107(1)
		Equatorial		2.9057(1), 2.8581(1)
	Bi–Br	Axial	Terminal Br	2.8796(1)
			Bridging Br	2.8031(1)
		Equatorial		2.8316(1), 2.8428(1)

Table S5. Fit parameters (obtained using the New Amorphous dispersion formula, Equation S1) for the primary oscillator describing the low-energy absorption feature in the plot of α vs. energy for **1-Tl** in the two unique orientations of 0° and 90° and **2-Tl$_{\mathbf{BA}}$**. (This is the oscillator defined as ω_1 in Figures S14-S16). The parameters f_1, ω_1, and Γ_1 describe the peak intensity, position, and breadth, respectively.

	1-Tl$_{\mathbf{0}}$	**1-Tl$_{\mathbf{90}}$**	**2-Tl$_{\mathbf{BA}}$**
f_1	0.019	0.022	0.031
ω_1	2.92	3.08	2.78
$\boldsymbol{\Gamma_1}$	**0.325**	**0.386**	**0.459**

Table S6. Fit parameters obtained from a Pseudo-Voigt fit (Equation S2) to the sharp low-energy peak in the plots of α vs. energy for **1-Bi** and **2-Bi**. The parameter *w* represents the full width at half maximum.

	1-Bi	**2-Bi**
y_0	2581.4452	-4590.76164
A	57261.96	72343.14537
μ	0.11241	0.79306
$\boldsymbol{w}$	**0.28703**	**0.28563**
x_c	3.03831	2.98799

Table S7. Calculated bandgaps of experimental structures. Bandgaps of $Cs_2TlAgBr_6$, **1-Tl**, **2-Tl$_{PEA}$**, **1′-Tl** and **1-In** were calculated with HSE06; those of **1-Bi** and **2-Bi** using PBE+SOC.

	Nature of the bandgap	*k*-points	Calculated bandgap (eV)
$Cs_2TlAgBr_6$	Direct	Γ	0.12
2-Tl$_{PEA}$	Direct	Γ	1.22
1-Tl	Indirect	$A^{VBM} \rightarrow B^{CBM}$	2.00
1′-Tl	Indirect	$V^{VBM} \rightarrow \Gamma^{CBM}$	2.17
1-In	Indirect	$A^{VBM} \rightarrow \Gamma^{CBM}$	3.30
1-Bi	Direct	Γ	1.76
2-Bi	Indirect	$A^{VBM} \rightarrow B^{CBM}$	1.66

Table S8. The lowest energy transitions between the given *k*-points of experimental and model structures as calculated with HSE06.

	k-points	HSE06 energy difference (eV)
1-Tl	$A^{VBM} \rightarrow B^{CBM}$	2.00
	$A^{VBM} \rightarrow \Gamma^{CB}$	2.13
	Γ	2.65
1M	$A^{VBM} \rightarrow B^{CB}$	1.84
	$A^{VBM} \rightarrow \Gamma^{CBM}$	1.65
	Γ	1.72
2-Tl$_{PEA}$	Γ	1.22
	$V^{VB} \rightarrow \Gamma^{CBM}$	1.24
2M	Γ	0.98
	$V^{VB} \rightarrow \Gamma^{CBM}$	1.04

Equation S1. Absorption coefficient (α) as a function of energy (ω) for a single oscillator according to the New Amorphous dispersion formula, which was used to model the ellipsometry data of **1-Tl** and **2-Tl$_{\mathrm{BA}}$**. The parameters f_j, ω_j, and Γ_j describe the peak intensity, position, and breadth, respectively, while ω_g is a fitting parameter that approximates the bandgap.

$$\alpha(\omega) = \frac{4\pi}{\lambda}\left[\frac{f_j\left(\omega-\omega_g\right)^2}{\left(\omega-\omega_j\right)^2+\Gamma_j^2}\right]$$

Equation S2. Pseudo-Voigt function used to fit the low-energy features in the ellipsometry spectra of **1-Bi** and **2-Bi**. The parameters y_0, A, w, and x_c describe the peak's y-offset, amplitude, full width at half max, and position respectively, and μ is the profile shape factor which describes the ratio of Gaussian to Lorentzian character used in the fit.

$$y = y_0 + A\left(\left[\frac{2\mu}{\pi}\right]\left[\frac{w}{4(x-x_c)^2+w^2}\right] + (1-\mu)\left[\frac{\sqrt{4\ln 2}}{w*\sqrt{\pi}}\right]e^{\left[\frac{-4\ln 2}{w^2}(x-x_c)^2\right]}\right)$$

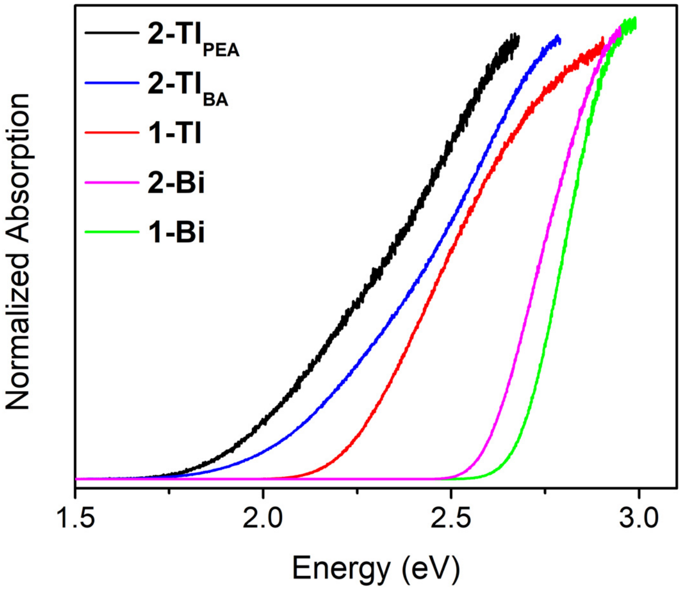

Figure S1. Kubelka-Munk transformed diffuse reflectance data of **2-Tl$_{\mathrm{PEA}}$**, **2-Tl$_{\mathrm{BA}}$**, **1-Tl**, **2-Bi**, and **1-Bi**. The absorption onset of **2-Tl$_{\mathrm{PEA}}$** and **2-Tl$_{\mathrm{BA}}$** are very similar. There is a much larger difference between the absorption onsets of **2-Tl$_{\mathrm{PEA/BA}}$** and **1-Tl** (ca. 0.33 eV) than between the absorption onsets of **2-Bi** and **1-Bi** (ca. 0.07 eV).

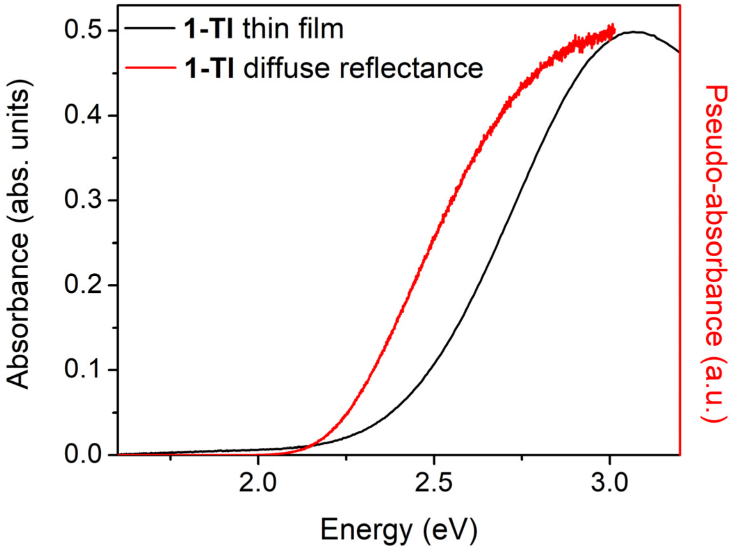

Figure S2. The absorption onset of **1-Tl** measured through thin-film transmission (black trace) and diffuse reflectance (red trace). Diffuse reflectance is sensitive to weak absorption events in the material not observable through thin-film transmission.

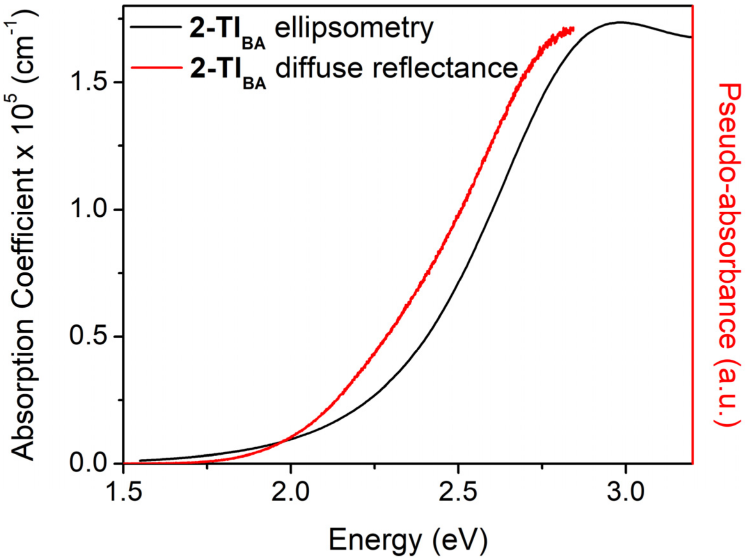

Figure S3. The absorption onset of **2-Tl$_{BA}$** measured through ellipsometery (black trace) and diffuse reflectance (red trace). Diffuse reflectance is sensitive to weak absorption events in the material not observable through ellipsometry.

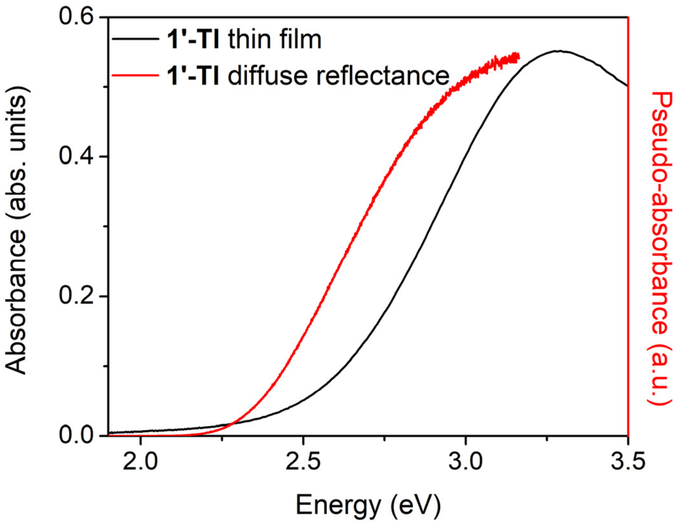

Figure S4. The absorption onset of **1′-Tl** measured through thin-film transmission (black trace) and diffuse reflectance (red trace). Diffuse reflectance is sensitive to weak absorption events in the material not observable through thin-film transmission.

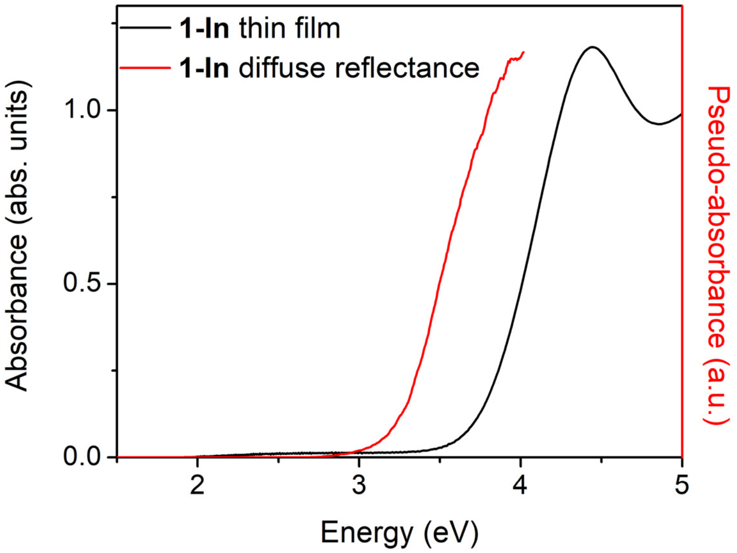

Figure S5. The absorption onset of **1-In** measured through thin-film transmission (black trace) and diffuse reflectance (red trace). Diffuse reflectance is sensitive to weak absorption events in the material not observable through thin-film transmission.

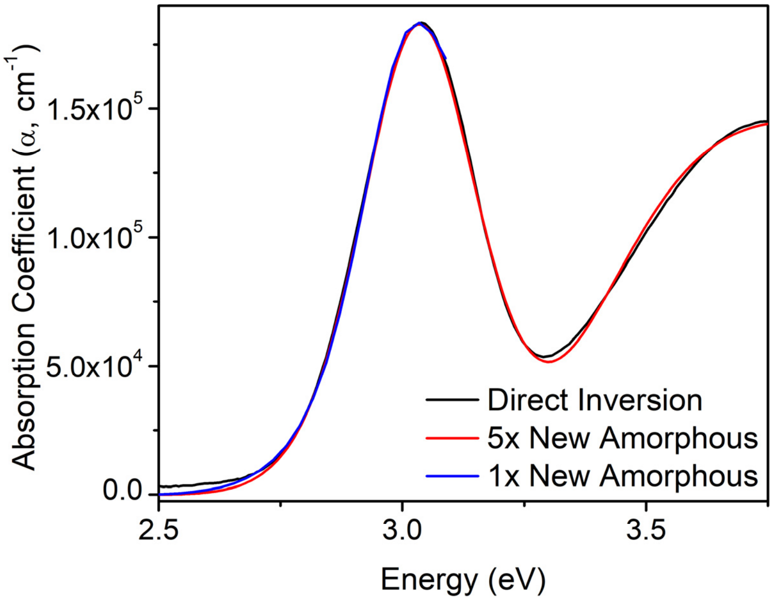

Figure S6. Comparison of the plot of α vs. energy of **1-Bi** obtained when three different modeling strategies were used. The black trace was obtained via direct inversion of the ellipsometric data. The red trace was obtained using the New Amorphous dispersion formula with five oscillators (note that here, some of the oscillators had unphysical (negative) parameters). The blue trace was obtained using the New Amorphous dispersion formula with one oscillator to only fit the low-energy portion of the data.

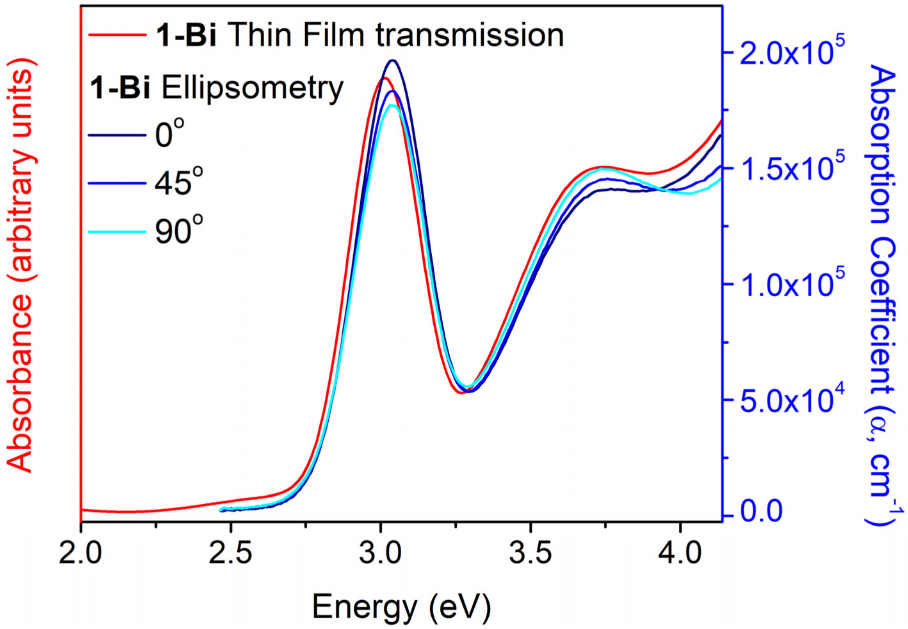

Figure S7. Plots of α vs. energy obtained from ellipsometry measurements on a single crystal of **1-Bi** in three different orientations. The ellipsometry data obtained in different orientations do not differ substantially. The thin-film transmission spectrum of a film of **1-Bi** is shown in red. Notably, there is good agreement between the absorption spectrum obtained via these two very different techniques.

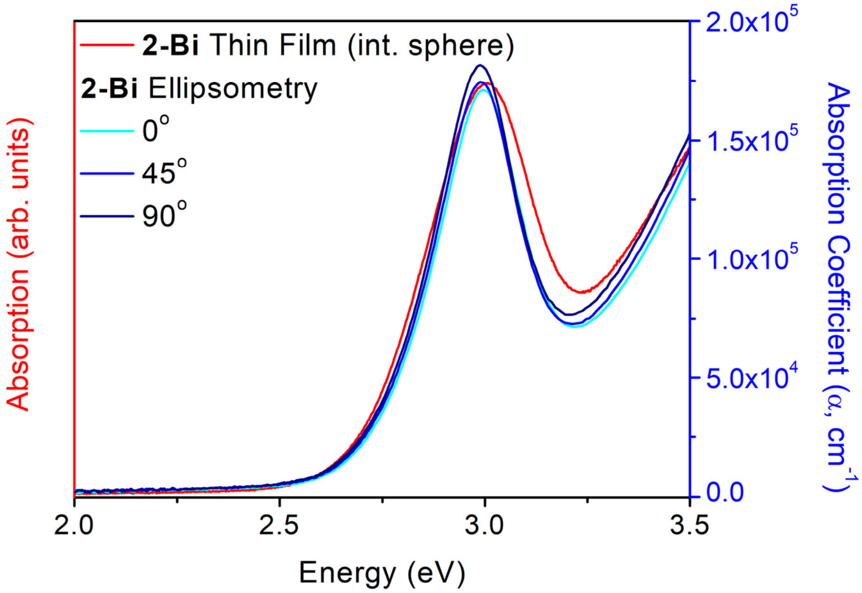

Figure S8. Plots of α vs. energy obtained from ellipsometry measurements on a single crystal of **2-Bi** in three different orientations. The ellipsometry data obtained in different orientations do not differ substantially. The absorption spectrum of a thin film of a film of **2-Bi** obtained using an integrating sphere is shown in red. Notably, there is good agreement between the absorption spectrum obtained via these two very different techniques.

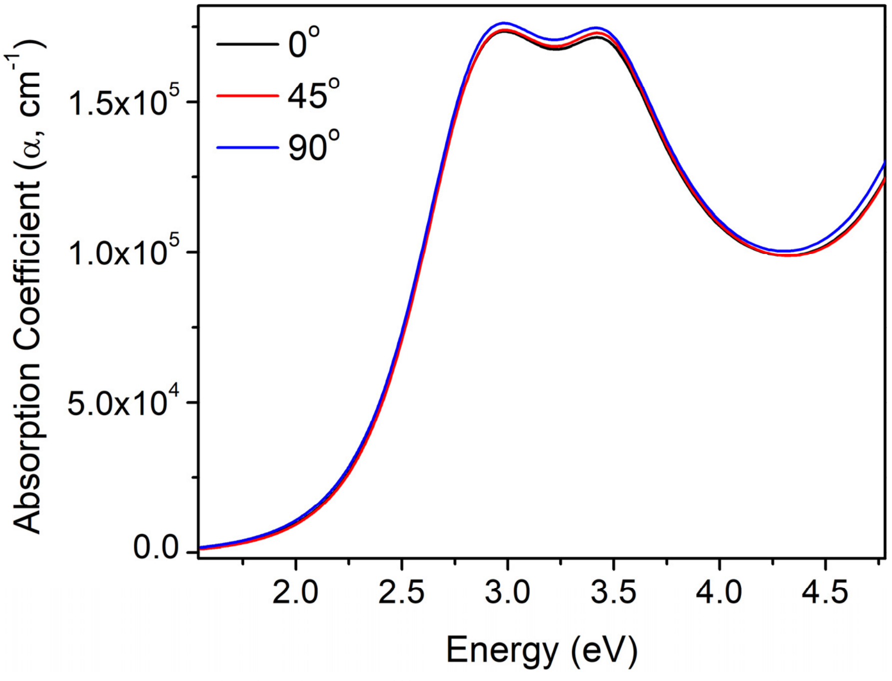

Figure S9. Plots of α vs. energy obtained from ellipsometry measurements on a single crystal of **2-Tl$_{\mathbf{BA}}$** in three different orientations. The ellipsometry data obtained in different orientations do not differ substantially.

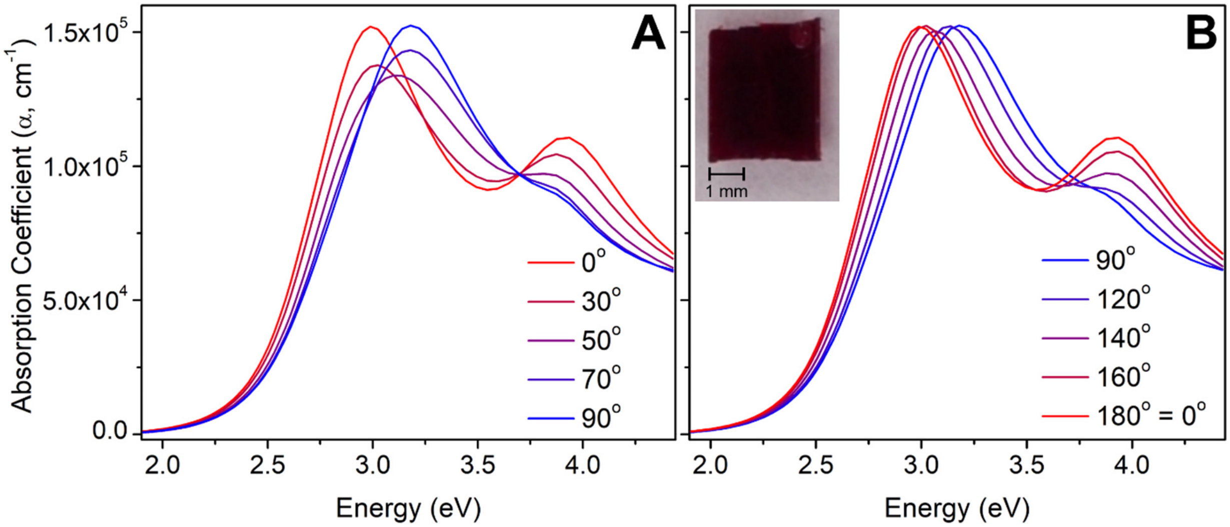

Figure S10. Plots of α vs. energy obtained upon rotating a crystal of **1-Tl** (B, inset) through 180°.

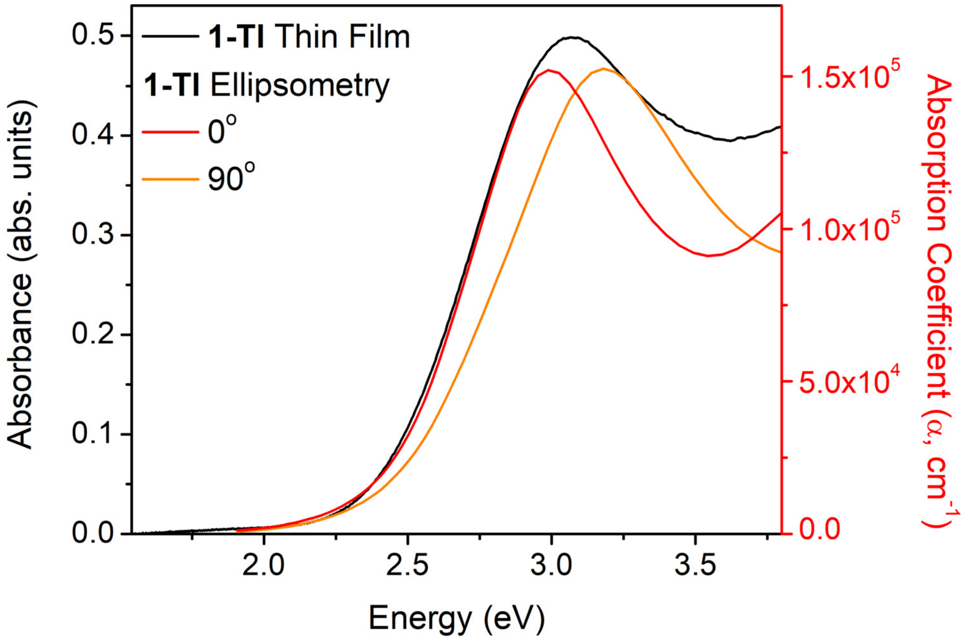

Figure S11. Plots of α vs. energy obtained from ellipsometry measurements of a crystal **1-Tl** in the two unique orientations defined in the main text (0° and 90°, red and orange traces, respectively). The thin-film transmission spectrum of **1-Tl** is also shown (black trace). Taken individually, neither trace matches the thin-film transmission spectrum well, although their average is a good match (Figure 3D).

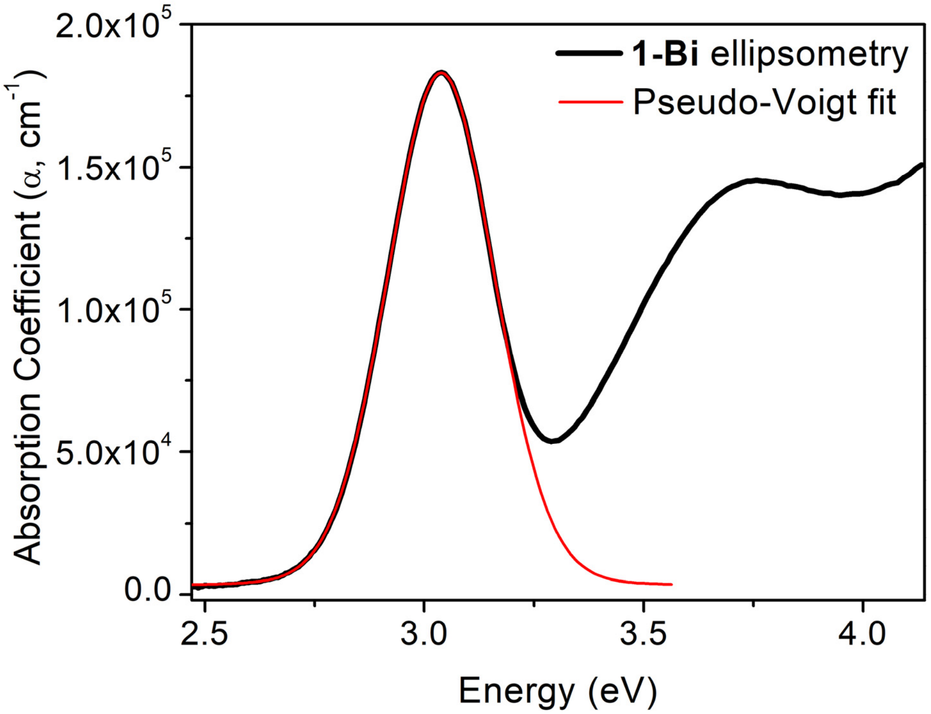

Figure S12. Plot of α vs. energy obtained from direct inversion of the ellipsometric data of **1-Bi** (black trace) and the Pseudo-Voigt fit to the sharp low-energy feature (red trace). The fit parameters are given in Table S6. See "Ellipsometry measurements" section above for full details

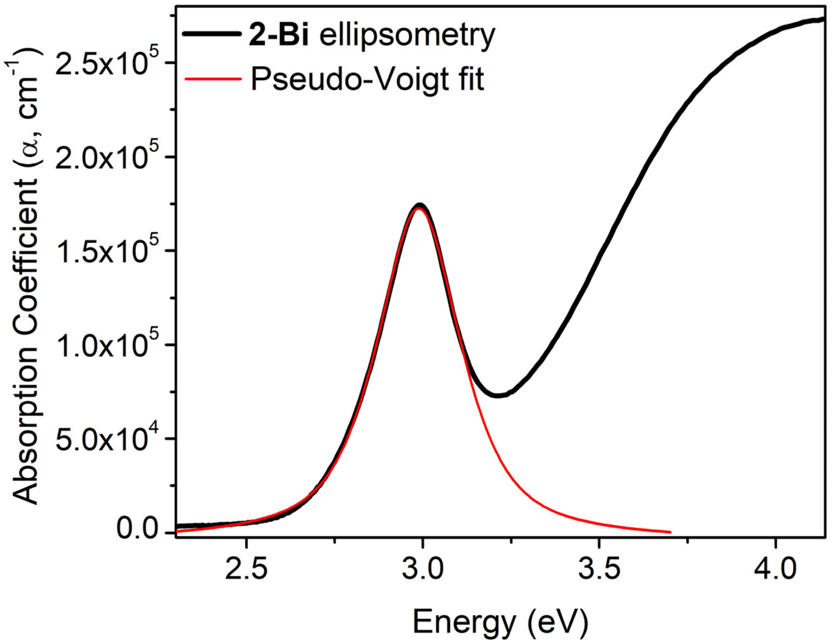

Figure S13. Plot of α vs. energy obtained from direct inversion of the ellipsometric data of **2-Bi** (black trace) and the Pseudo-Voigt fit to the sharp low-energy feature (red trace). The fit parameters are given in Table S6. See "Ellipsometry measurements" section above for full details

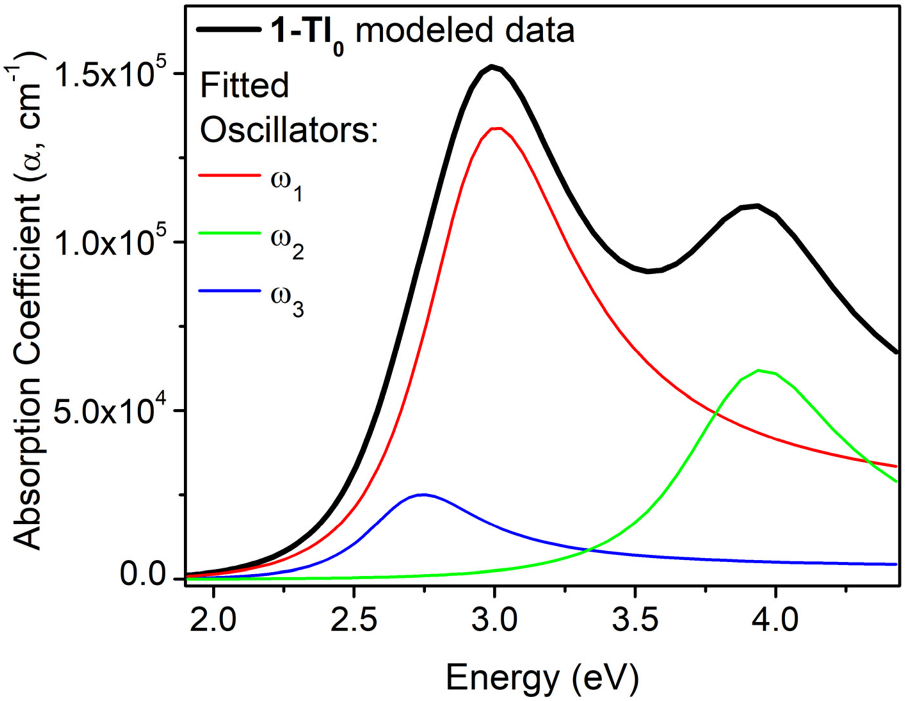

Figure S14. Three major oscillators used to fit the experimental ellipsometric data of **1-Tl$_0$** (colored traces) and the modeled spectrum (the sum of the oscillators used to fit the data; black trace). The peak parameters for ω$_1$ are given in Table S5. See "Ellipsometry measurements" section above for full details.

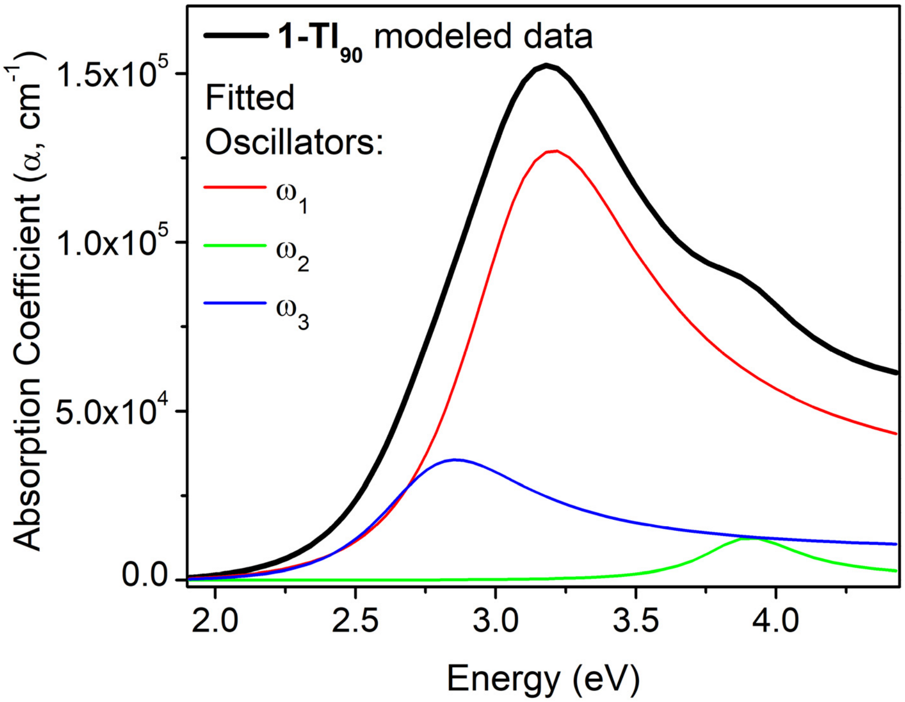

Figure S15. Three major oscillators used to fit the experimental ellipsometric data of **1-Tl$_{90}$** (colored traces) and the modeled spectrum (the sum of the oscillators used to fit the data; black trace). The peak parameters for ω$_1$ are given in Table S5. See "Ellipsometry measurements" section above for full details.

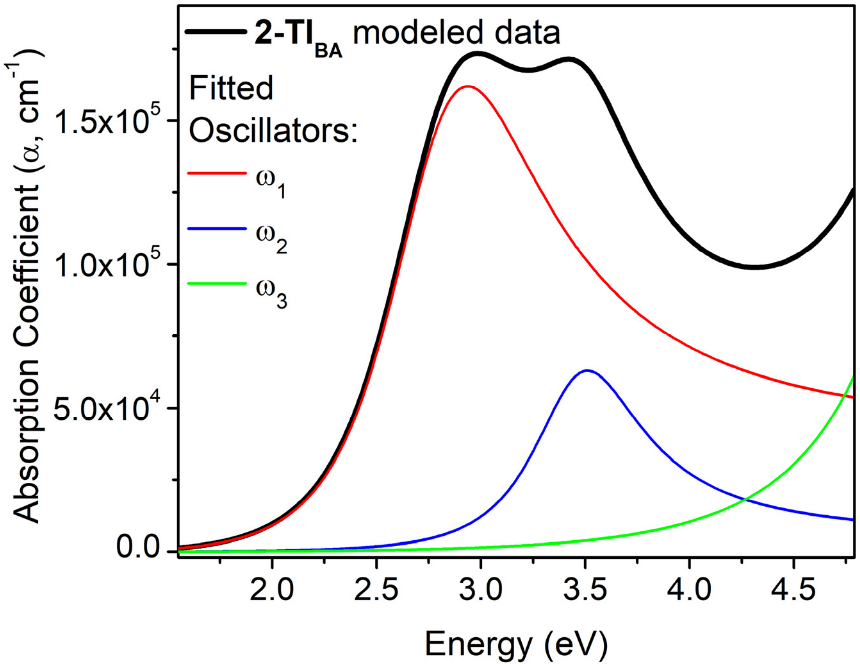

Figure S16. Three major oscillators used to fit the experimental ellipsometric data of **2-Tl$_{BA}$** (colored traces) and the modeled spectrum (the sum of the oscillators used to fit the data; black trace). The peak parameters for ω_1 are given in Table S5. See "Ellipsometry measurements" section above for full details.

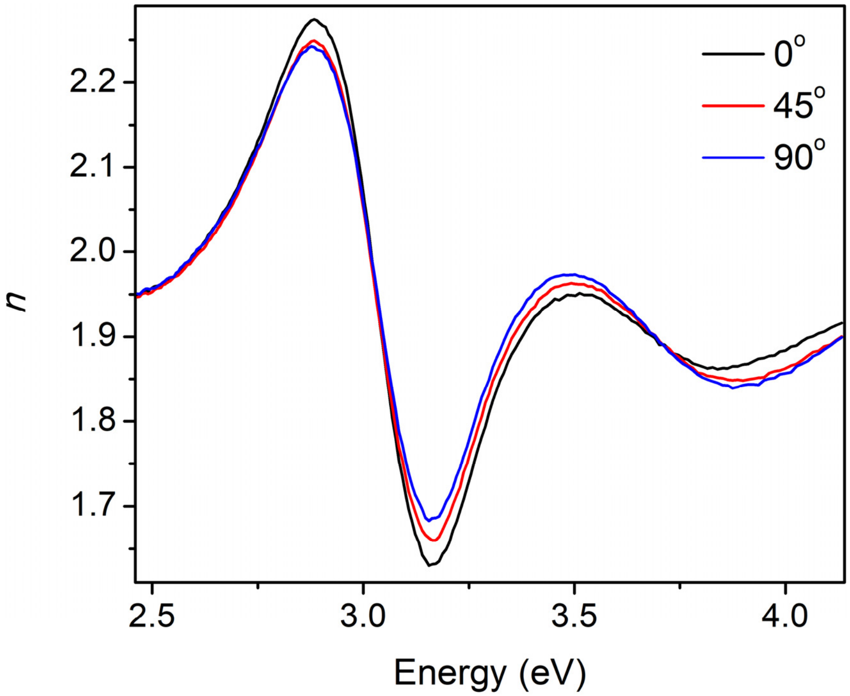

Figure S17. Plots of refractive index (*n*) vs. energy obtained from ellipsometry measurements on a single crystal of **1-Bi** in three different orientations. The data presented here and in Figure S7 were extracted from the same ellipsometry measurements.

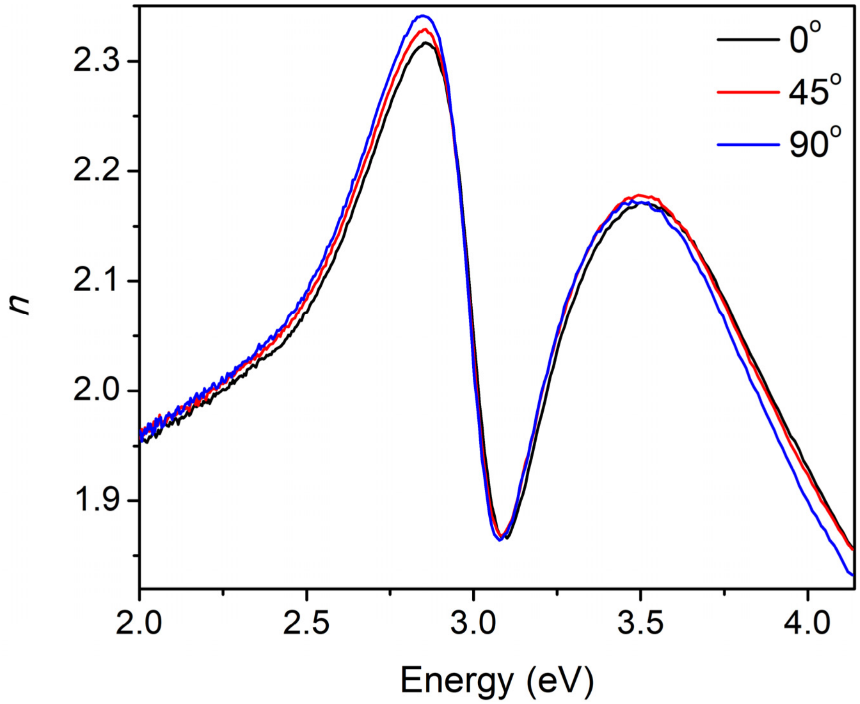

Figure S18. Plots of refractive index (*n*) vs. energy obtained from ellipsometry measurements on a single crystal of **2-Bi** in three different orientations. The data presented here and in Figure S8 were extracted from the same ellipsometry measurements.

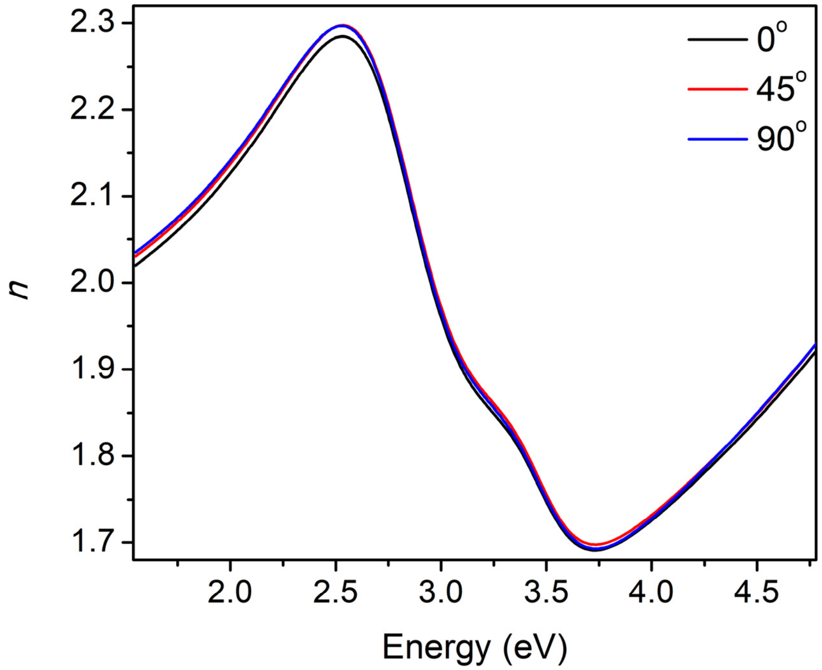

Figure S19. Plots of refractive index (*n*) vs. energy obtained from ellipsometry measurements on a single crystal of **2-Tl$_{\mathbf{BA}}$** in three different orientations. The data presented here and in Figure S9 were extracted from the same measurements.

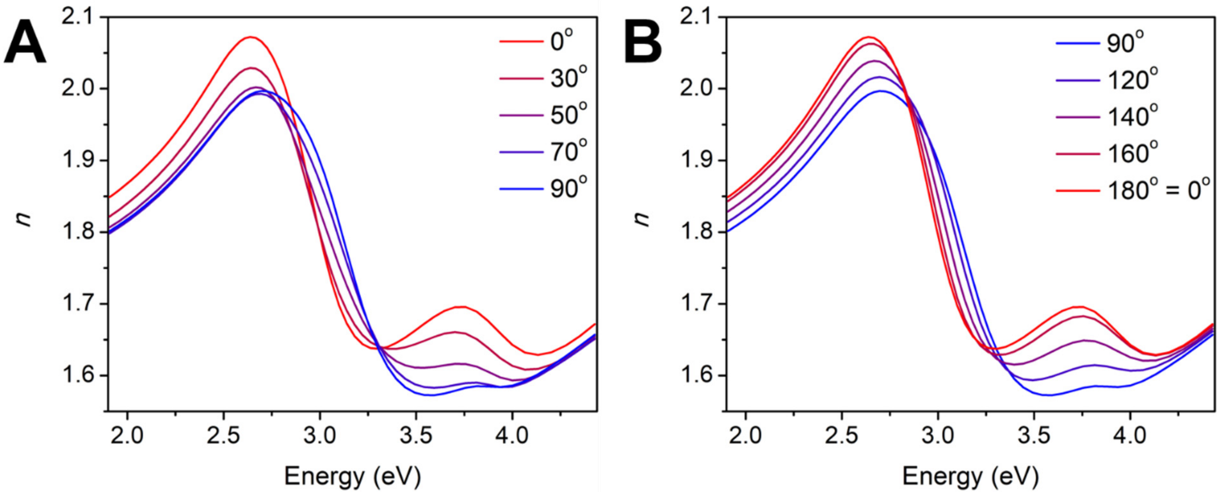

Figure S20. Plots of refractive index (n) vs. energy obtained upon rotating a crystal of **1-Tl** through 180°. The data presented here and in Figure S10 were extracted from the same measurements.

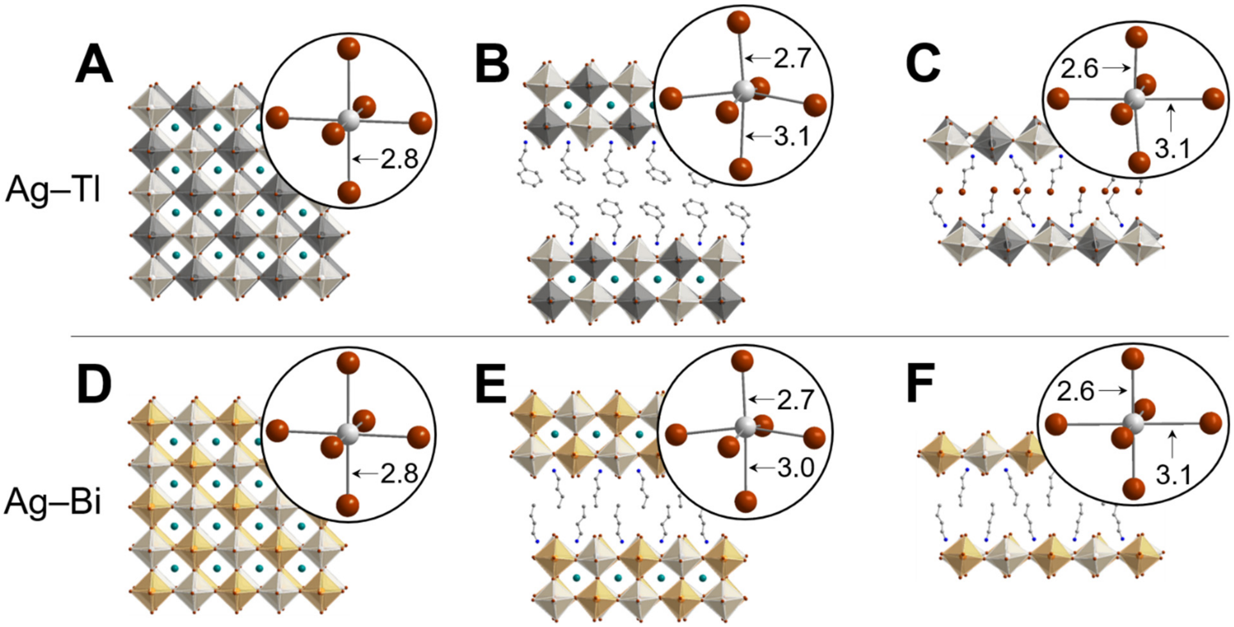

Figure S21. Structures of the 3D, $n = 2$, and $n = 1$ Ag–Tl (A, B, and C, respectively) and Ag–Bi (D, E, and F, respectively) perovskites with insets showing the coordination environment about the Ag site in each material. The distortions of the Ag–Br octahedra are quite similar in both perovskite families. See Tables S3 and S4 for additional structural parameters. White, black, orange, brown, teal, gray, and blue spheres represent Ag, Tl, Bi, Br, Cs, C, and N atoms, respectively. H and disordered atoms omitted for clarity.

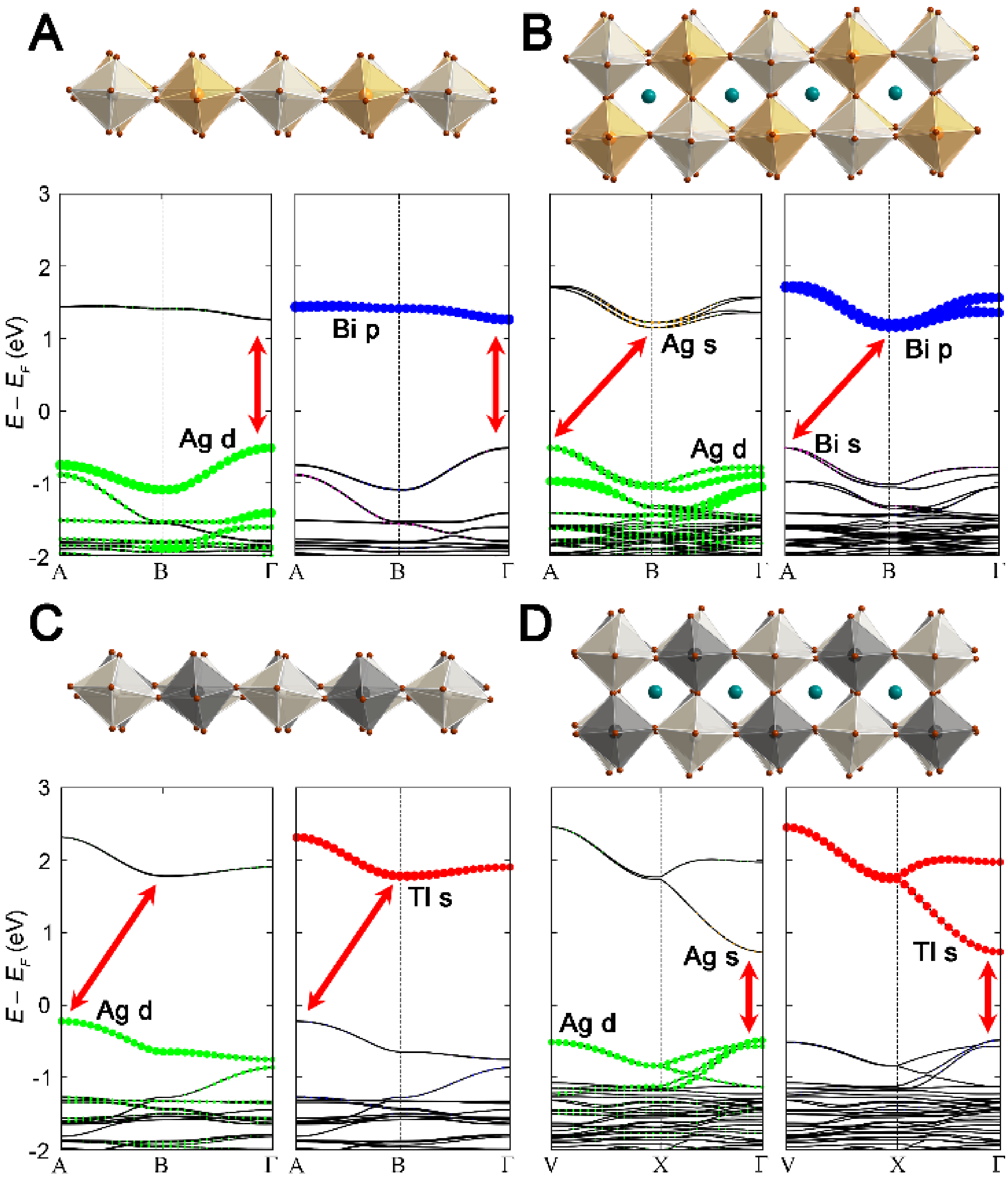

Figure S22. Electronic band structures of (A) **1-Bi**, (B) **2-Bi**, (C) **1-Tl**, and (D) **2-Tl**$_{\mathrm{PEA}}$ calculated from the SCXRD structures. White, black, orange, brown, and teal spheres represent Ag, Tl, Bi, Br, and Cs atoms, respectively. Band structures are shown in duplicate with Ag and Bi (A and B) or Tl (C and D) orbital contributions denoted by the size of the colored circles in the left and right panels, respectively. Halide orbital contributions are present throughout but not shown for clarity.

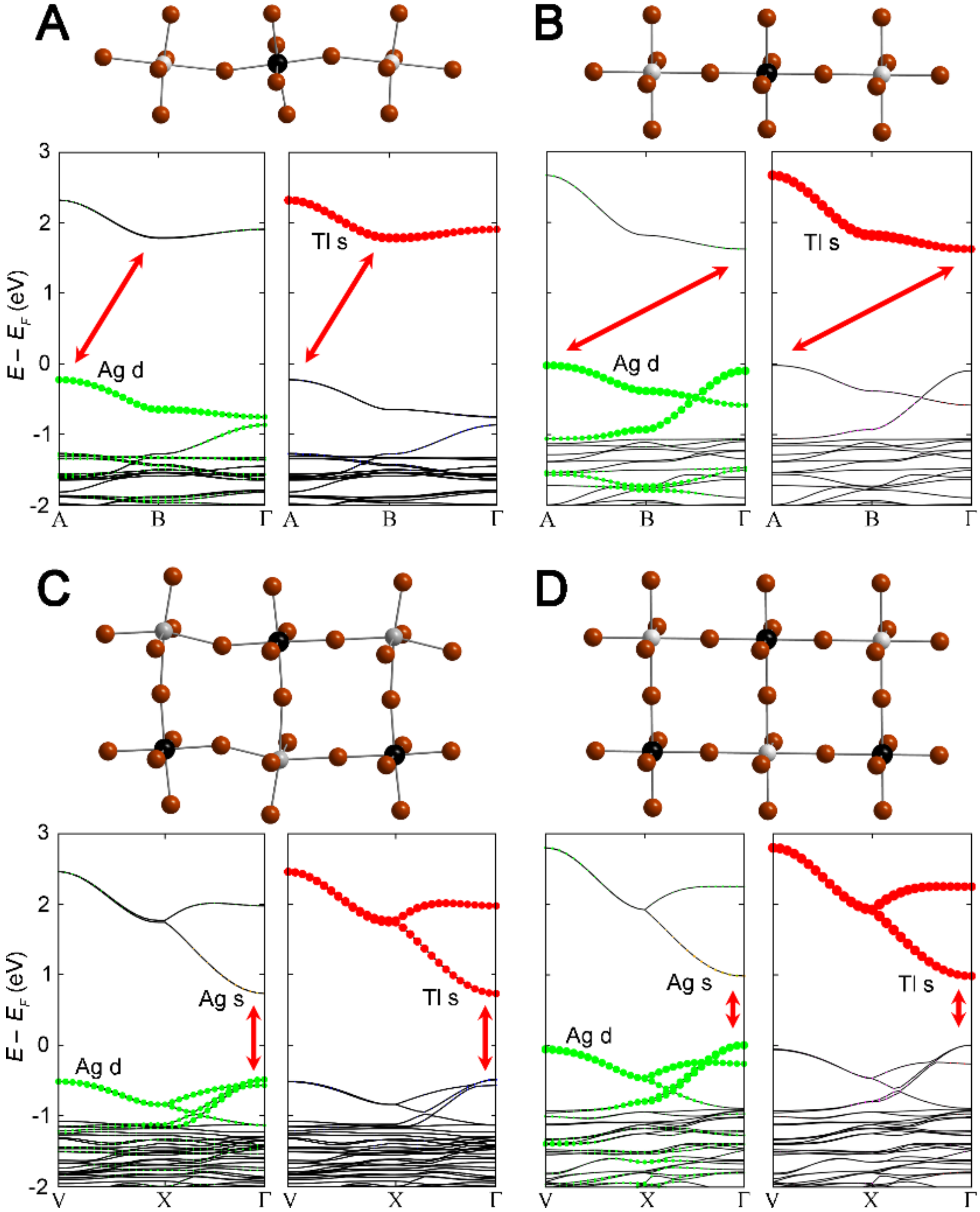

Figure S23. Band structures calculated from the experimental n = 1 (**1-Tl**, A), undistorted model n = 1 (**1M**, B), experimental n = 2 (**2-Tl$_{\mathbf{PEA}}$**, C), and undistorted model n = 2 (**2M**, D) structures of the Ag-Tl perovskites. Gray, black, and brown spheres represent Ag, Tl, and Br atoms, respectively. Band structures are shown in duplicate with Ag and Tl orbital contributions denoted by the size of the colored circles in the left and right panels, respectively. Halide orbital contributions are present throughout but not shown for clarity.

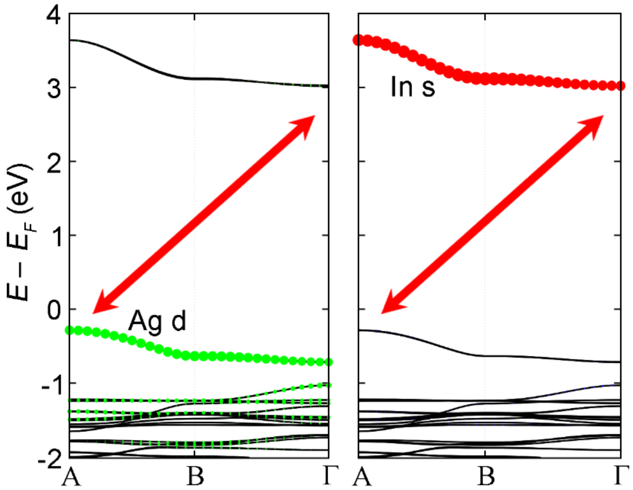

Figure S24. Band structure of **1-In** showing the indirect bandgap between A in the valence band and Γ in the conduction band. The metal-orbital character of each band is denoted by colored dots and the dot size is proportional to the degree of orbital participation. The band structure is shown in duplicate with Ag and In orbital contributions denoted by the size of the colored circles in the left and right panels, respectively. Halide orbital contributions are present throughout but not shown for clarity.

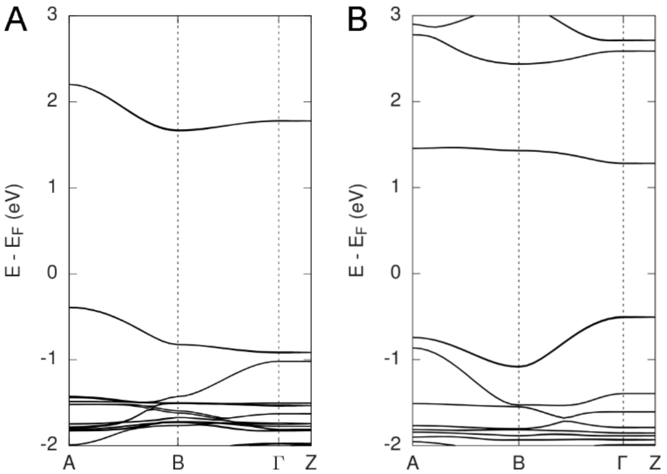

Figure S25. Band structures of **1-Tl** (A) and **1-Bi** (B) displaying the Z point (reciprocal space coordinates of (0, 0, $^{\pi}/_{c}$) in order to demonstrate the lack of dispersion along the Γ→Z direction as expected for a 2D material.

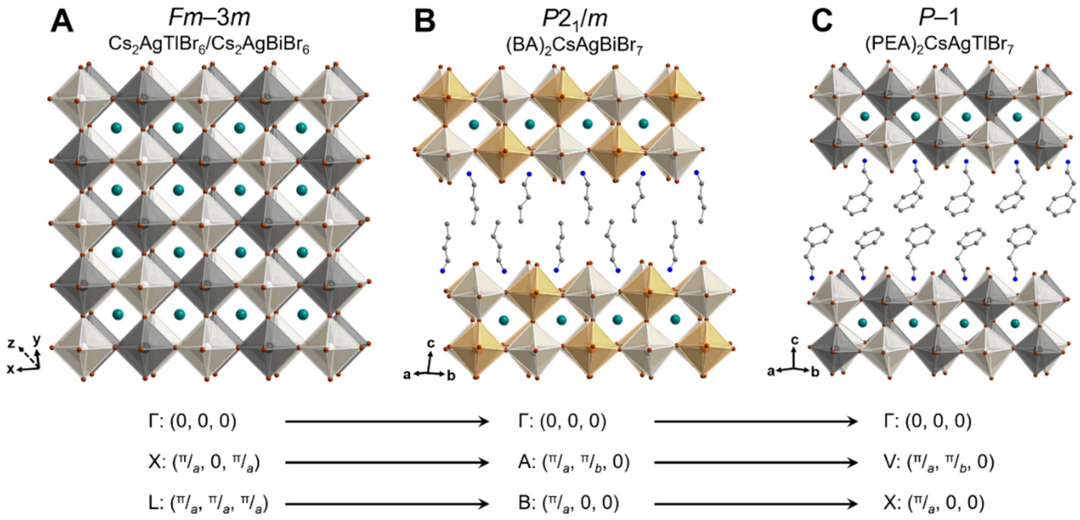

Figure S26. We previously demonstrated that the X and L points of the *Fm*–3*m* lattice of 3D $Cs_2AgBiBr_6$ are the translational symmetry equivalents of the A and B points, respectively, of the *P*2$_1$/*m* lattice of 2D **2-Bi**. Here we extend this derivation to show that the V and X points of the *P*–1 lattice of **2-Tl$_{PEA}$** are equivalent to the X and L points, respectively, of 3D $Cs_2AgTlBr_6$. In other words, the A and B points in the *P*2$_1$/*m* lattice have been relabeled as V and X, respectively, under *P*–1 symmetry. White, black, orange, brown, teal, blue, and gray spheres represent Ag, Tl, Bi, Br, Cs, N, and C atoms, respectively. Hydrogen and disordered atoms omitted for clarity.

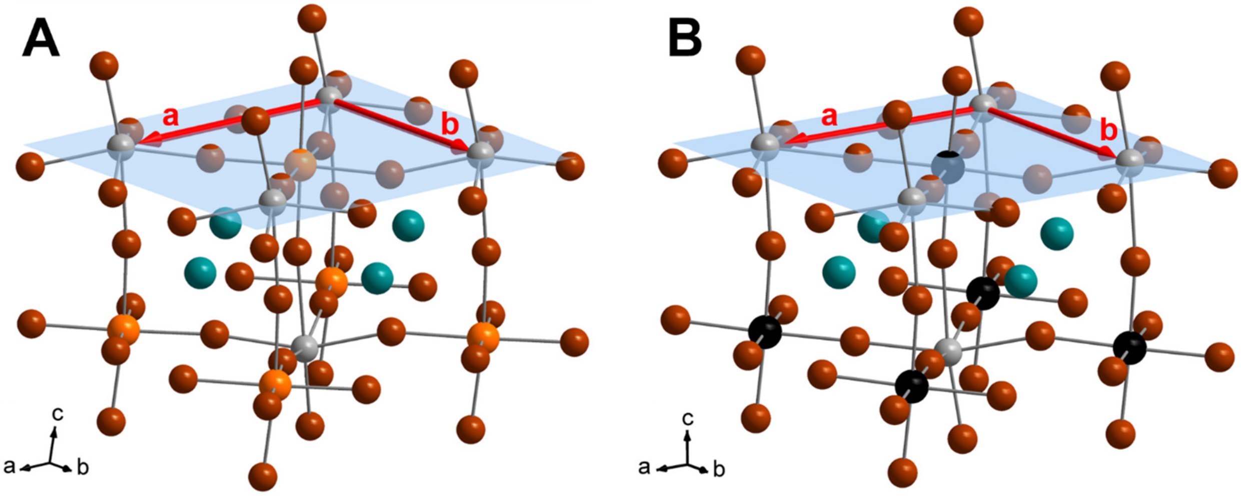

Figure S27. Illustration of the in-plane (**a** and **b**) unit-cell vectors of **2-Bi** and **2-Tl$_{PEA}$** showing the analogy of these vectors between the two materials. In both cases, the vectors bisect Br–M–Br bonds, pointing between metal centers of the same type. Gray, black, orange, brown, and teal spheres represent Ag, Tl, Bi, Br, and Cs atoms, respectively.

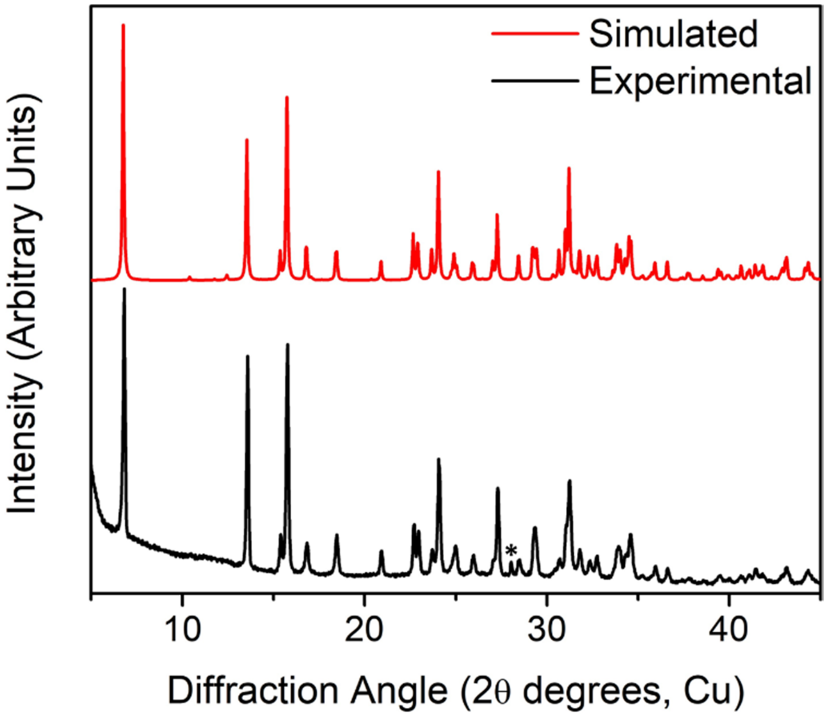

Figure S28. Powder XRD pattern of *n* = 1 $(3\text{-BPA})_4AgInBr_8$ (**1-In**) and the pattern simulated from the room-temperature single-crystal data. The peak at 2θ = 28° marked with an asterisk is due to the sample holder.

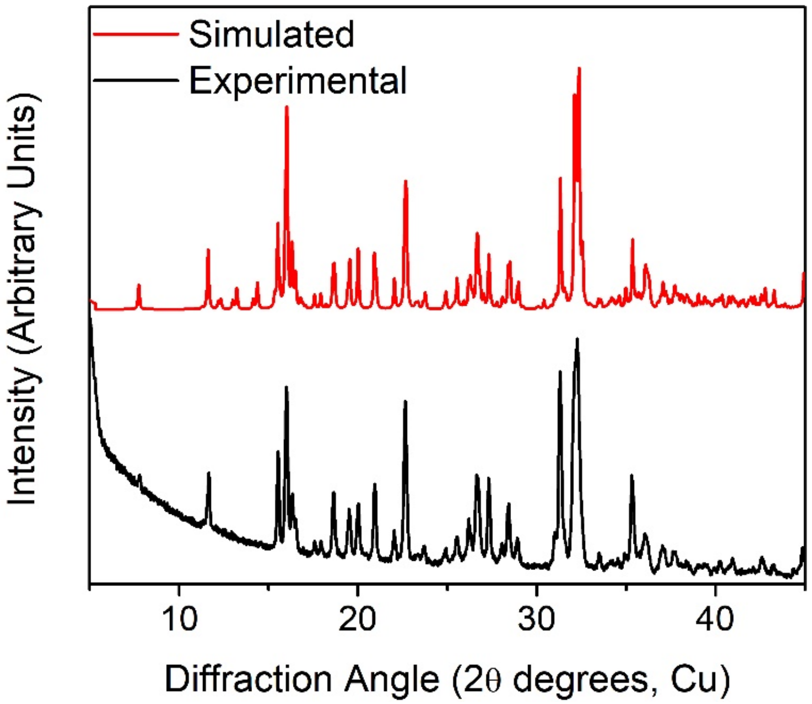

Figure S29. Powder XRD pattern of *n* = 2 $(PEA)_2CsAgTlBr_7$ (**2-Tl$_{PEA}$**) and the pattern simulated from the room-temperature single-crystal data.

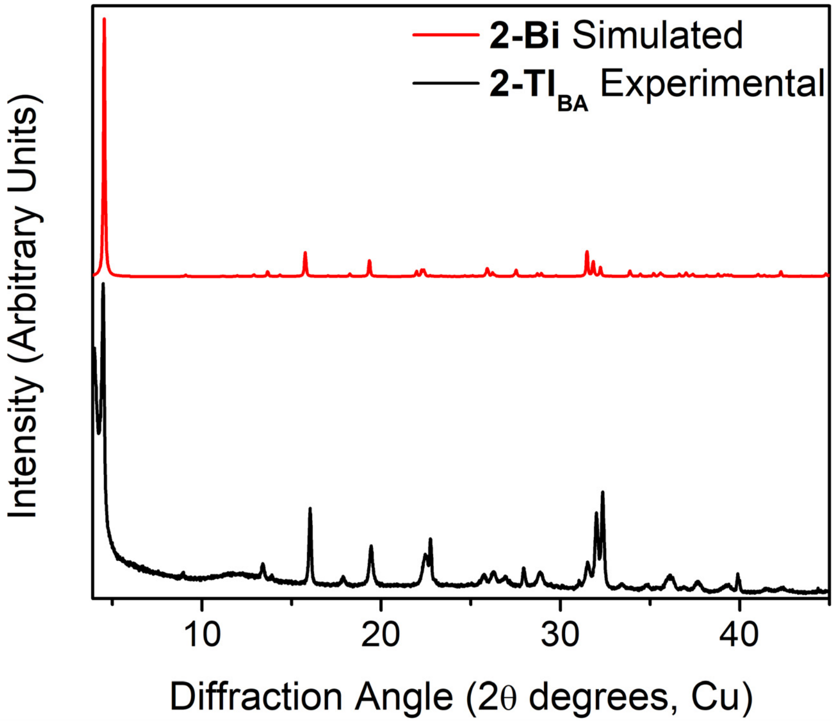

Figure S30. Powder XRD pattern of *n* = 2 $(BA)_2CsAgTlBr_7$ (**2-Tl$_{BA}$**) and the pattern simulated from the room-temperature single-crystal data of $(BA)_2CsAgBiBr_7$ (**2-Bi**). The similarity of these patterns is consistent with our expectation that **2-Tl$_{BA}$** has a structure very similar to that of **2-Bi**.

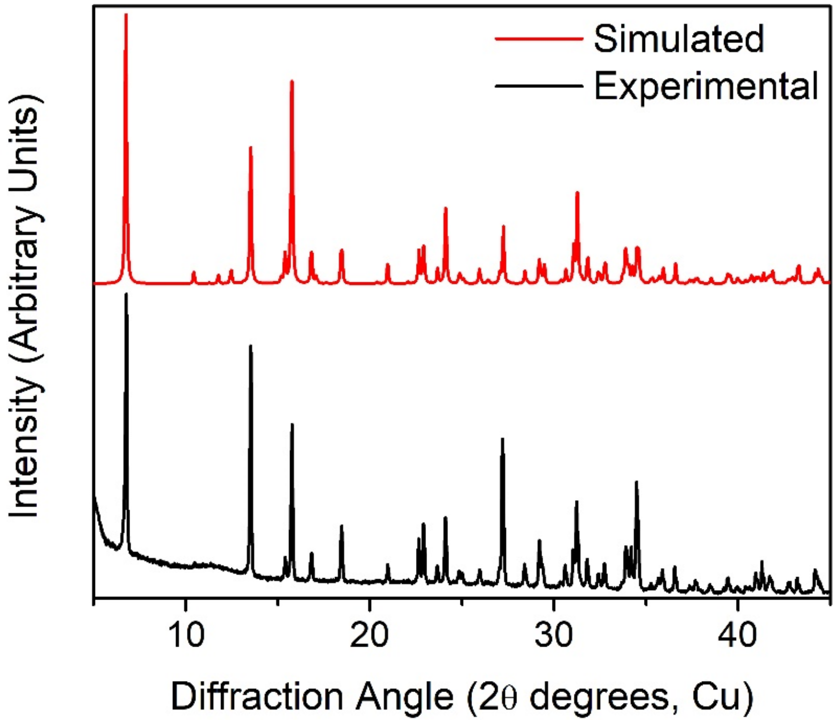

Figure S31. Powder XRD pattern of *n* = 1 $(3\text{-}BPA)_4AgTlBr_8$ (**1-Tl**) and the pattern simulated from the room-temperature single-crystal data.

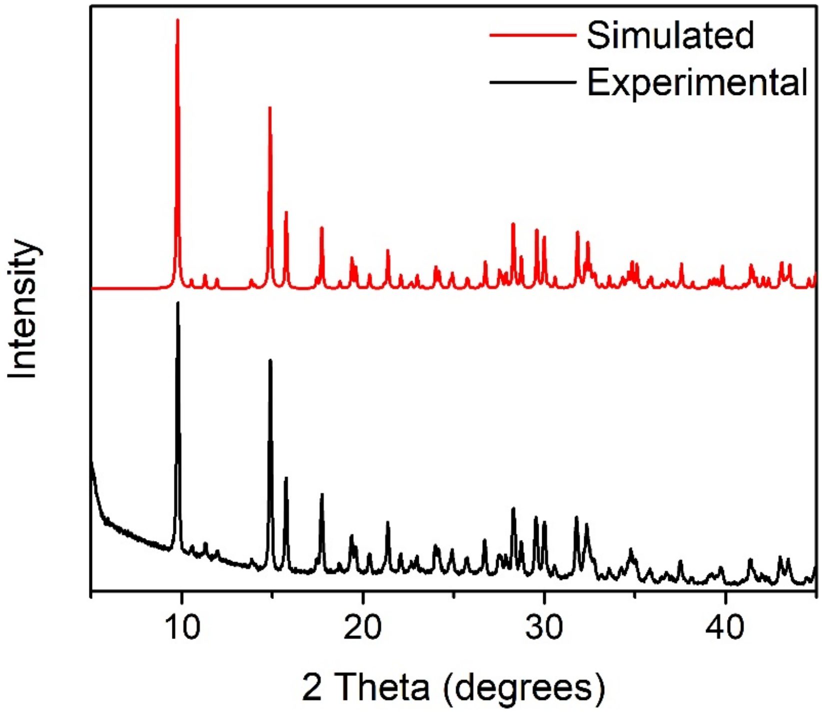

Figure S32. Powder XRD pattern of *n* = 1 $(HIS)_2AgTlBr_8$ (**1′-Tl**) and the pattern simulated from the room-temperature single-crystal data.

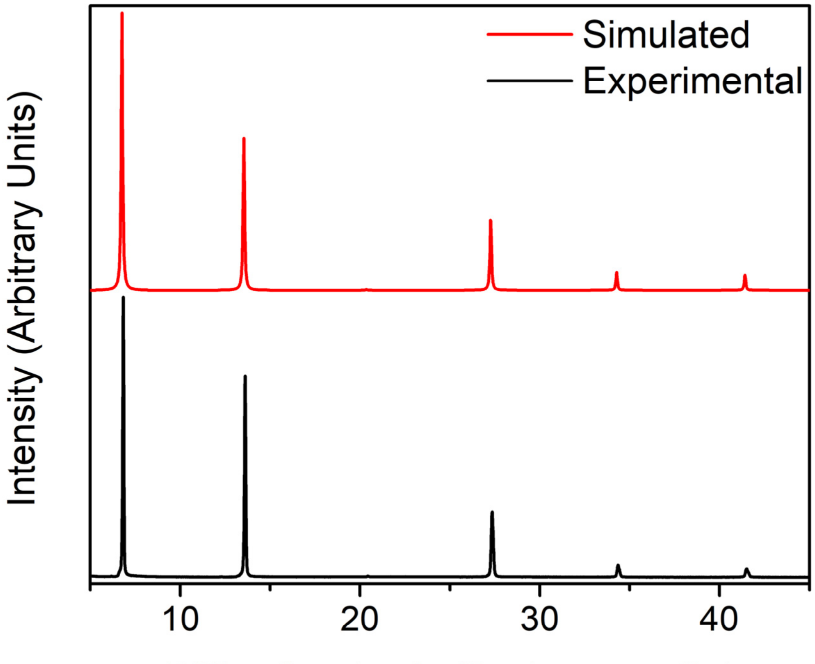

Figure S33. PXRD pattern of a film of *n* = 1 $(3\text{-BPA})_4AgInBr_8$ (**1-In**) and the pattern simulated from the room-temperature single-crystal data of **1-In** assuming (001) preferred orientation.

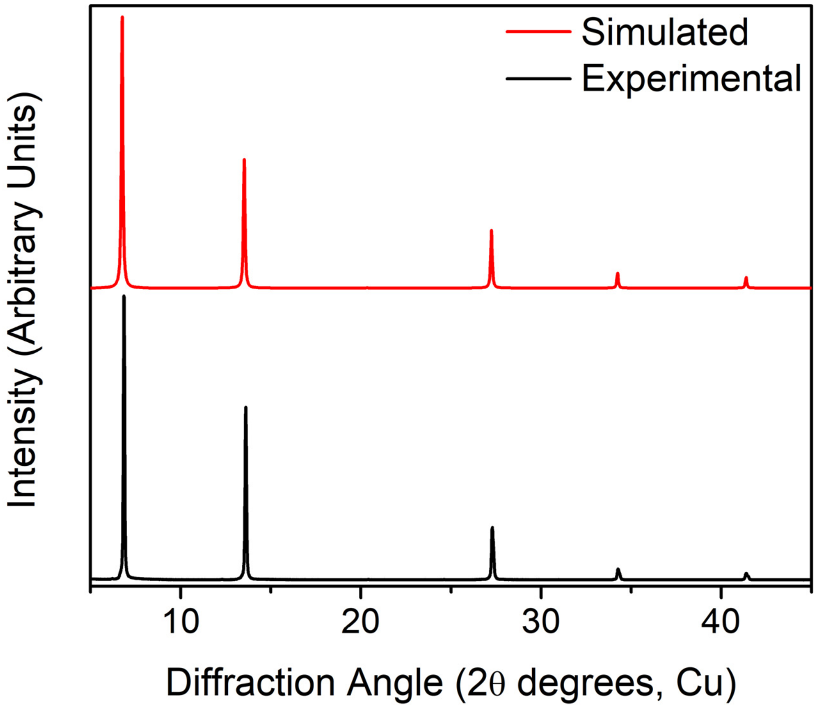

Figure S34. PXRD pattern of a film of $n = 1$ (3-BPA)$_4$AgTlBr$_8$ (**1-Tl**) and the pattern simulated from the room-temperature single-crystal data of **1-Tl** assuming (001) preferred orientation.

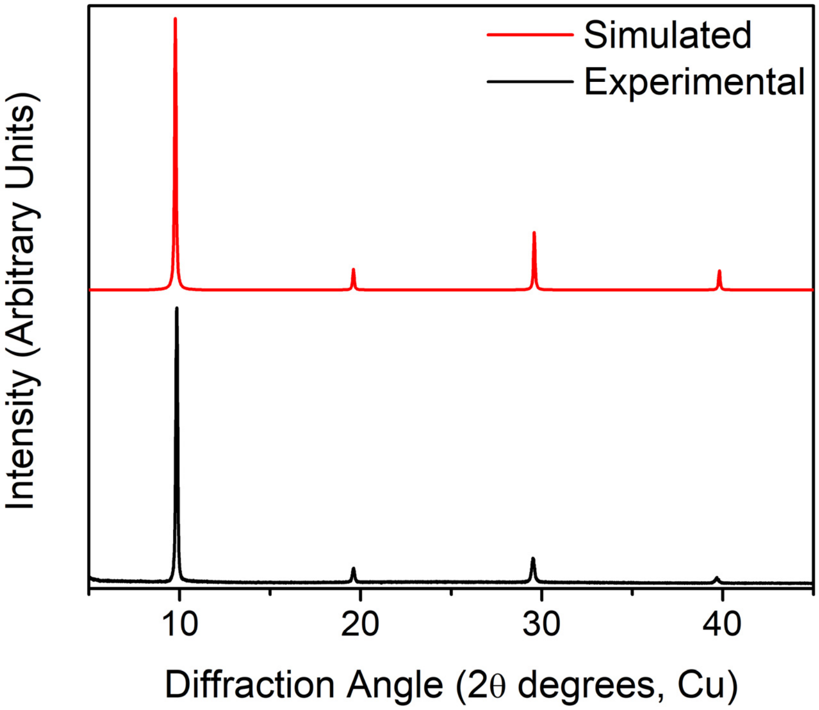

Figure S35. PXRD pattern of a film of (HIS)$_2$AgInBr$_8$ (**1′-Tl**) and the pattern simulated from the room-temperature single-crystal data of **1′-Tl** assuming (001) preferred orientation.

References

1. D. E. Rusyniak, in *Clinical Neurotoxicology: Syndromes, Substances, Environments*, ed. M. R. Dobbs, Saunders Elsevier, Philadelphia, 2009, ch. 24, pp. 277-281.
2. B. A. Connor, L. Leppert, M. D. Smith, J. B. Neaton and H. I. Karunadasa, *J. Am. Chem. Soc.*, 2018, **140**, 5235-5240.
3. *SAINT and SADABS*, Bruker AXS Inc.: Madison, Wisconsin, 2007.
4. G. M. Sheldrick, *SHELXL-97, A program for crystal structure refinement*, Göttingen, 1997.
5. G. M. Sheldrick, *Acta Crystallogr., Sect. A: Found. Crystallogr.*, 2008, **64**, 112-122.
6. O. V. Dolomanov, L. J. Bourhis, R. J. Gildea, J. A. K. Howard and H. Puschmann, *J. Appl. Crystallogr.*, 2009, **42**, 339-341.
7. P. Müller, R. Herbst-Irmer, A. L. Spek, T. R. Schneider and M. R. Sawaya, *Crystal Structure Refinement: A Crystallographer's Guide to SHELXL*, Oxford University Press, New York, 2006.
8. P. Kubelka and F. Munk, *Z. Tech. Phys.*, 1931, **12**, 593-603.
9. A. H. Slavney, L. Leppert, A. Saldivar Valdes, D. Bartesaghi, T. J. Savenije, J. B. Neaton and H. I. Karunadasa, *Angew. Chem. Int. Ed.*, 2018, **57**, 12765-12770.
10. J. Tauc, *Mat. Res. Bull.*, 1968, **3**, 37-46.
11. G. Kresse and J. Hafner, *Phys. Rev. B*, 1993, **47**, 558-561.
12. G. Kresse and J. Furthmüller, *Phys. Rev. B*, 1996, **54**, 11169-11186.
13. J. Klimeš, M. Kaltak and G. Kresse, *Phys. Rev. B*, 2014, **90**, 075125.
14. J. P. Perdew, K. Burke and M. Ernzerhof, *Phys. Rev. Lett.*, 1996, **77**, 3865-3868.
15. A. V. Krukau, O. A. Vydrov, A. F. Izmaylov and G. E. Scuseria, *J. Chem. Phys.*, 2006, **125**, 224106.
16. L. Leppert, T. Rangel and J. B. Neaton, *Phys. Rev. Materials*, 2019, **3**, 103803.
17. A. Tkatchenko and M. Scheffler, *Phys. Rev. Lett.*, 2009, **102**, 073005.
18. G. Volonakis, A. A. Haghighirad, R. L. Milot, W. H. Sio, M. R. Filip, B. Wenger, M. B. Johnston, L. M. Herz, H. J. Snaith and F. Giustino, *J. Phys. Chem. Lett.*, 2017, **8**, 772-778.